Elsevier Editorial System(tm) for Ceramics International
Manuscript Draft

Manuscript Number: CERI-D-15-00274R1

Title: Microstructural, mechanical and tribological properties of nanostructured YSZ coatings produced with different APS process parameters

Article Type: Full Length Article

Keywords: plasma spraying; hardness; Young's modulus; wear resistance; zirconia; thermal applications

Corresponding Author: Dr. Giovanni Di Girolamo,

Corresponding Author's Institution:

First Author: Caterina Lamuta

Order of Authors: Caterina Lamuta; Giovanni Di Girolamo; Leonardo Pagnotta

Abstract: Plasma sprayed ceramic coatings can be used in turbine engines as thermal barrier or abradable coatings, in order to improve the durability of the components as well as the efficiency. The presence of nanostructures, deriving from partial melting of agglomerated nanostructured particles, represents an interesting technological solution in order to improve their functional characteristics. In this work nanostructured yttria stabilized zirconia (YSZ) coatings were deposited by air plasma spraying (APS). The influence of the main process parameters on their microstructural, mechanical and tribological properties was investigated by scanning electron microscopy (SEM), indentation techniques at micro- and nano-scale and wear tests, respectively. Their porous microstructure was composed of well melted overlapped splats and partially melted nanostructured areas. This bimodal microstructure led to a bimodal distribution of the mechanical properties. An increase of plasma power and spraying distance was able to produce denser coatings, with lower content of embedded nanostructures, which exhibited higher elastic modulus and hardness as well as lower wear rate.

Detailed Response to Reviewers

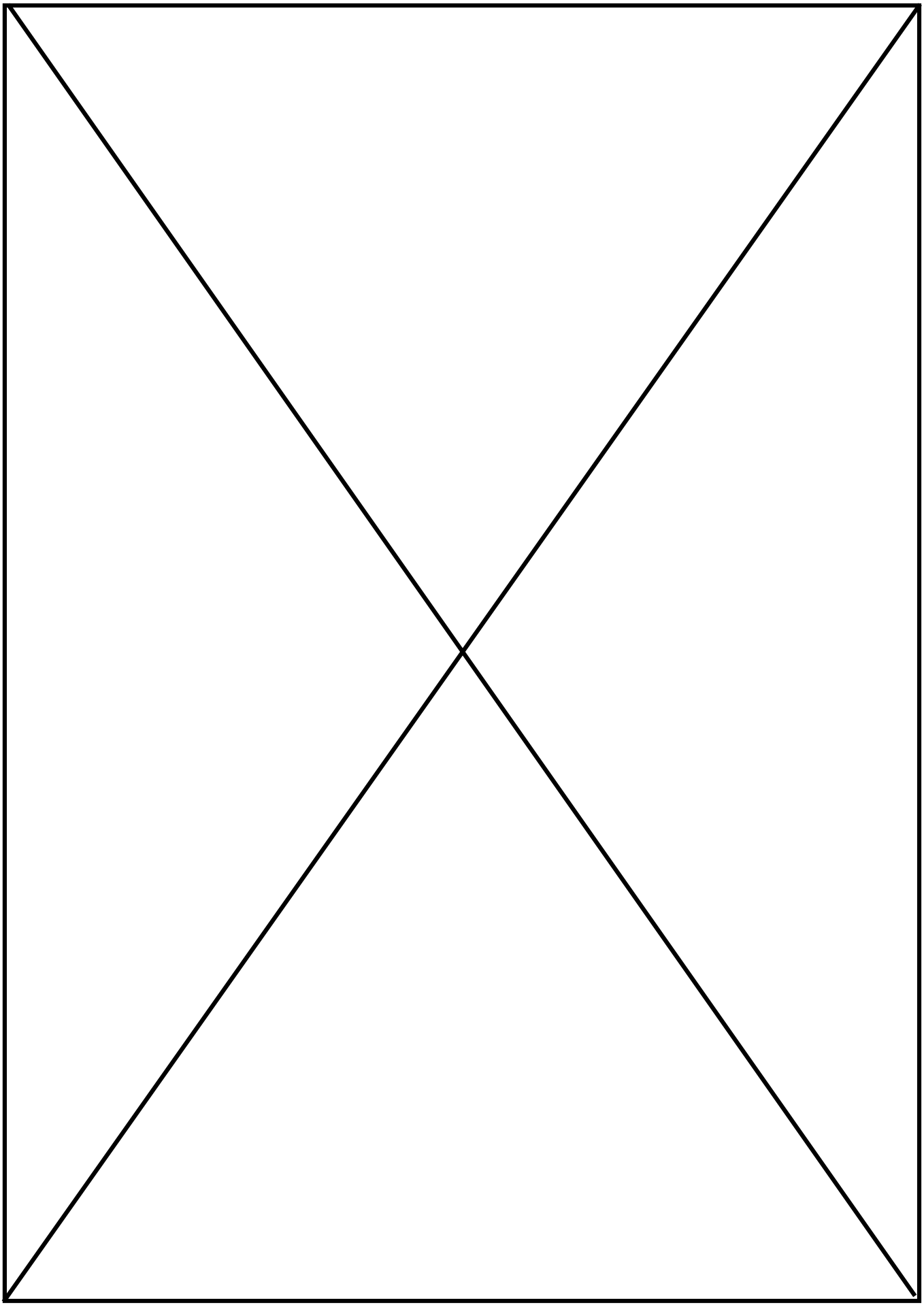

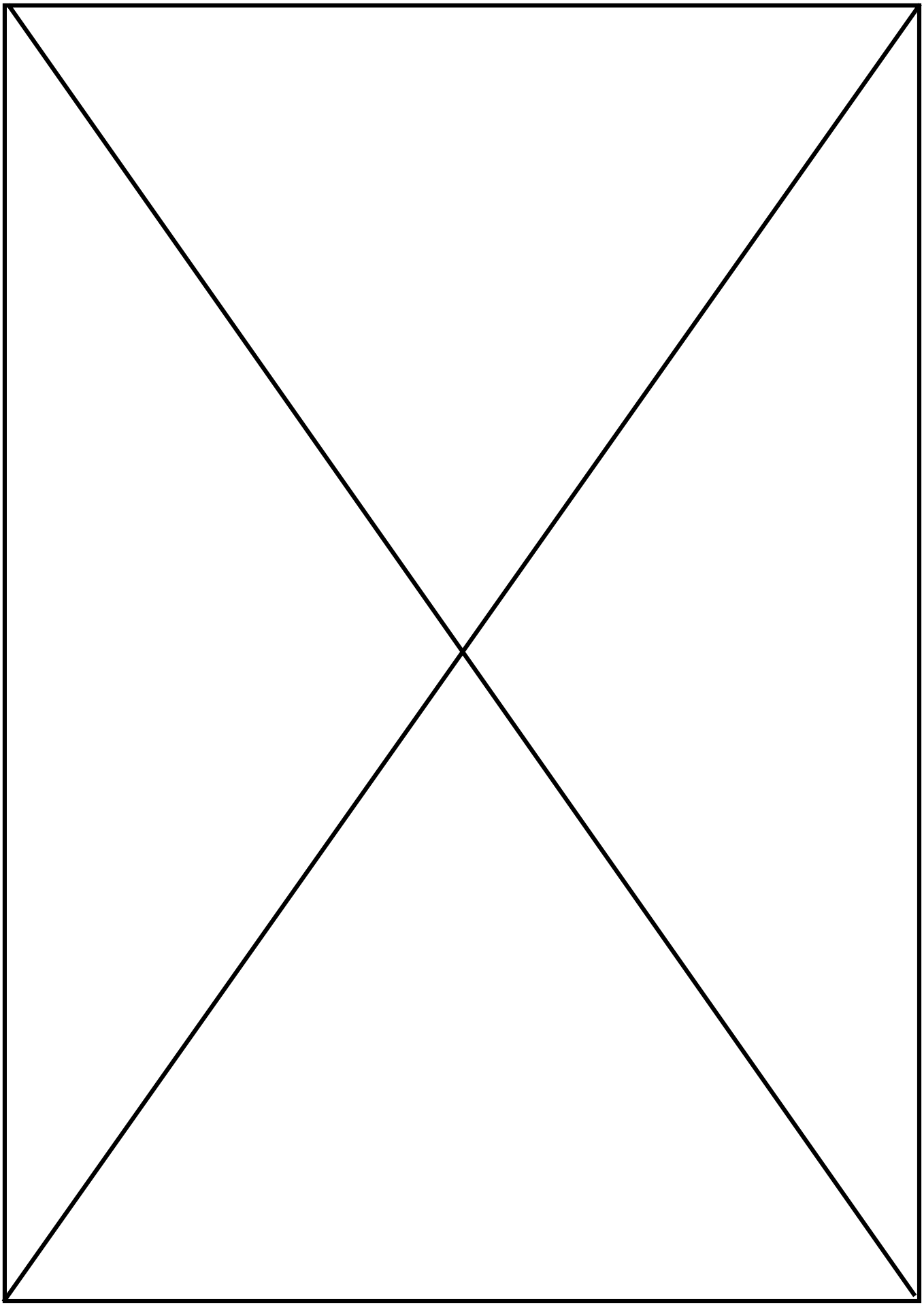

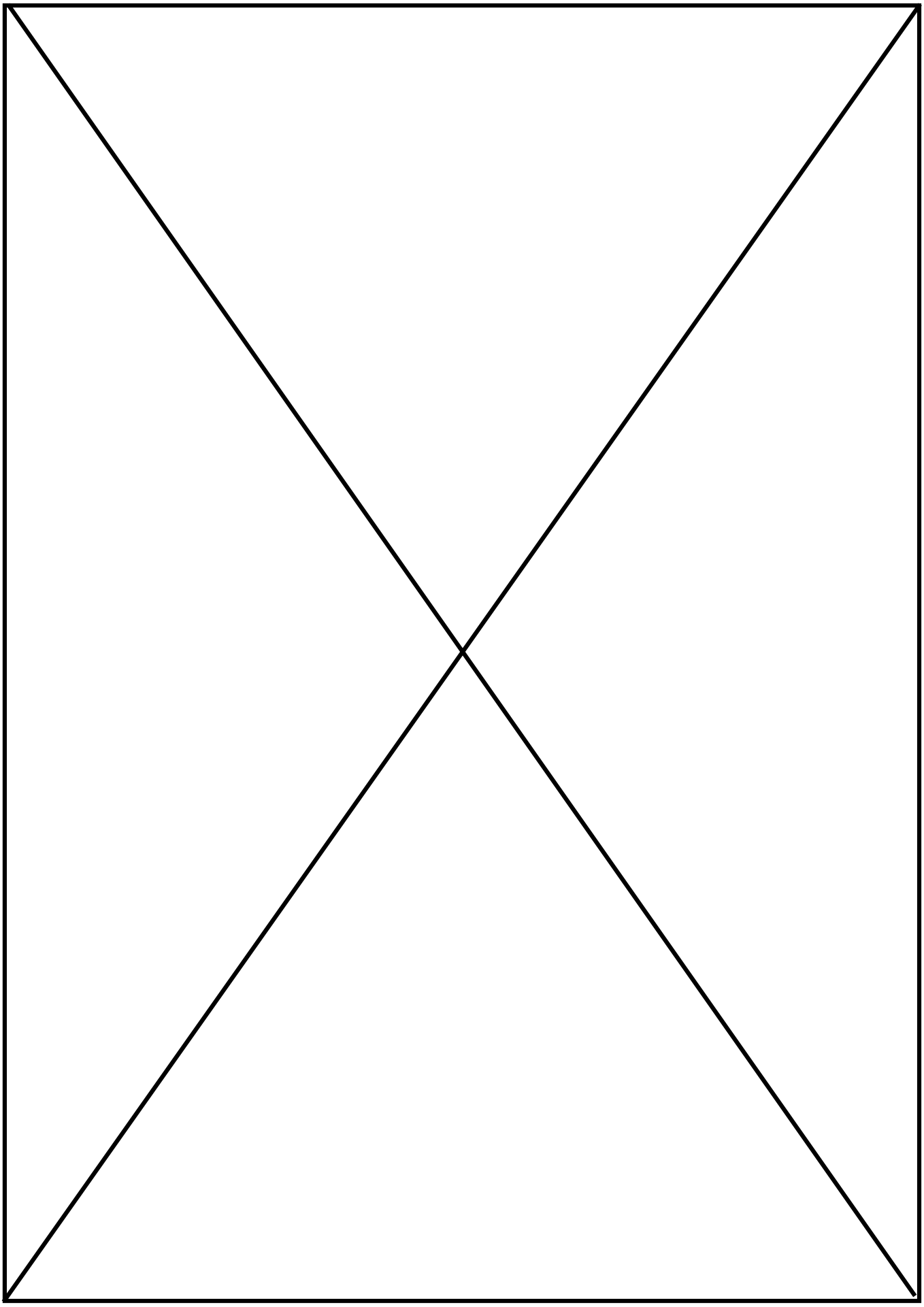

Microstructural, mechanical and tribological properties of nanostructured YSZ coatings produced with different APS process parameters

C. Lamuta[a], G. Di Girolamo [b,*], L. Pagnotta[a]

[a] Department of Mechanical Engineering, University of Calabria, Ponte P. Bucci, Cubo 44C, Rende, Italy

[b] ENEA, Materials Technology Unit, Casaccia Research Centre, Rome, Italy

[*] corresponding author: giovanni.digirolamo@enea.it

Abstract

Plasma sprayed ceramic coatings can be used in turbine engines as thermal barrier or abradable coatings, in order to improve the durability of the components as well as the efficiency. The presence of nanostructures, deriving from partial melting of agglomerated nanostructured particles, represents an interesting technological solution in order to improve their functional characteristics. In this work nanostructured yttria stabilized zirconia (YSZ) coatings were deposited by air plasma spraying (APS). The influence of the main process parameters on their microstructural, mechanical and tribological properties was investigated by scanning electron microscopy (SEM), indentation techniques at micro- and nano-scale and wear tests, respectively. Their porous microstructure was composed of well melted overlapped splats and partially melted nanostructured areas. This bimodal microstructure led to a bimodal distribution of the mechanical properties. An increase of plasma power and spraying distance was able to produce denser coatings, with lower content of embedded nanostructures, which exhibited higher elastic modulus and hardness as well as lower wear rate.

Keywords: A. plasma spraying; C. hardness; Young's modulus; B. wear resistance; D. zirconia; E. thermal applications

1. Introduction

Ceramic coatings are suitable to be employed for thermal protection of Ni-based superalloy turbine components operating in power plants and aircraft engines. Their application allows to improve their high-temperature capability and durability, by reducing the heat flux and the temperature at the metal surface. Significant improvements in terms of engine efficiency and lower pollution are then expected [1,2]. A thermal barrier coating (TBC) system is usually composed of a metal substrate, a metallic bond coat and a ceramic top coat [3]. The intermediate bond coat (MCrAlY) plays a meaningful role on the adhesion of the ceramic top coat and provides better resistance to the attack tipically promoted by oxygen and molten salts in severe working environments [4].

Ceramic materials with low thermal conductivity and heat capacity are good TBC candidates. Partially-yttria stabilized zirconia (8YSZ) is the most common used TBC material, owing to its satisfactory thermal and mechanical properties (low thermal conductivity, relatively high thermal expansion coefficient, low Young's modulus, high hardness and toughness) [5,6].

Plasma spraying is suitable for fabrication of thick porous coatings on complex metal parts. In such process powder particles are injected in the plasma jet by an inert gas, melted and accellerated toward the substrate, where they impact at high speed and quench, thus producing the build-up of a coating with typical microstructural defects such as splat boundaries, pores and microcracks [7].

During service at high temperature the infiltration of oxygen through the microcracks and interconnected pinholes of the ceramic TBC and the outward diffusion of bond coat constituents, such as Al, Cr and Ni, lead to the oxidation of the bond coat surface and to the following formation of the TGO (thermally grown oxide) at the interface. The gradual growth of the TGO layer assists the evolution of tensile stresses and the growth of horizontal cracks at the interface, thus leading to TBC spallation and to the failure of the whole TBC system [8,9]. To this purpose it has been reported that the use of nanostructured materials is able to promote the formation of a thin, uniform and dense TGO, partially suppressing the fast growth of other mixed oxides, reducing the oxidation rate and prolonging the lifetime of TBC systems exposed at 1000 °C and 1150 °C under cycling

conditions [10,11]. Indeed, the mixed oxides are usually characterized by high brittleness and microcrack growth.

Concerning ceramic TBCs it has been reported that significant enhancements can be achieved by using nanostructured materials in substitution of conventional ones. Indeed, the reduction of the grain size typically involves better mechanical strength and toughness [12,13]. The nanostructured coatings are characterized by higher interlamellar strength, *i.e*. the lamellae are well bonded each other in comparison with the conventional coatings owing to better filling and compactness between at splat boundary, as well as by higher crack propagation resistance, because the nanozones typically embedded within the microstructure act as crack arresters. The high porosity of nanostructured coatings also involves better thermal properties and thermal shock characteristics [12].

It is worth noting that single nanoparticles cannot be carried by plasma jet and deposited on the substrate, so that they are commonly pre-synthesized in micronsized particle agglomerates. To this purpose, these agglomerates should be only partially melted to preserve part of their starting nanostructure. On the contrary, if the agglomerates are totally melted, the grain growth occurs and the final microstructure resembles that of a conventional coating [14].

In the present work different process parameters were employed for coating manufacturing in order to control the degree of melting of the powder particles and to obtain coatings with well-tailored characteristics. The morphology and the microstructure of nanostructured YSZ coatings were investigated by scanning electron microscopy (SEM). Nano and Micro Indentation (NI, MI) tests were employed to study the evolution of the main mechanical properties, such as Young's modulus and hardness, whereas the wear rate was obtained by means of a ball-on-disk test. A statistical approach was used to study the mechanical properties of YSZ coatings and their relationship with the microstructure.

2. Experimental procedure

2.1 Plasma spraying

YSZ ceramic coatings were deposited on Ni superalloy disks (IN738, □ = 25 mm, thickness = 4 mm). The substrates were sand blasted using an alumina abrasive powder to increase their surface roughness and to improve the mechanical interlocking between coating and substrate. The substrate roughness, measured using three dimensional optical surface profilometer, was found to be 6.9 ± 1.1 μm. An atmospheric plasma spraying equipment, with 4F-MB plasma torch with 6 mm internal diameter nozzle, was used for coating deposition. A metallic CoNiCrAlY coating (Amdry 995C, Sulzer Metco) with thickness of 150 μm was previously applied as bond coat on the substrate surface.

Nanostructured partially yttria stabilized zirconia TBCs were then deposited using the nanostructured ZrO_2-7wt% Y_2O_3 powder feedstock (Nanox S4007, Inframat, US). The final thickness of the coatings was of about 300 μm whereas their roughness was equal to 8.3 ± 1.0 μm (no significant changes were appreciated for the samples produced using different process parameters). Two sets of six different samples were produced. The six samples of each set differ for the process parameters employed: the arc current was varied on three levels (500 A, 565 A and 630 A) and the substrate-torch distance on two levels (80 mm e 100 mm). The other parameters were kept constant and can be summarized as follows: primary gas flow rate (Ar) 40 slpm, secondary gas flow rate (H_2) 12 slpm, powder flow rate 28.5 g/min, substrate tangential speed 2086 mm/s.

2.2 Microstructure

The phase composition of nanostructured zirconia powder and coatings produced using different processing parameters was investigated by x-ray powder diffractometer (XRD PW 1880, Philips, Almelo, Netherlands) operating with CuKα radiation (λ = 0.154186 nm) produced at 40 kV and 40

mA. The analyzed range of the diffraction angle 2θ was between 20 and 80°, by a step width of 0.02° and a time per step equal to 5 s.

The morphology and the microstructure of powder feedstock and as-sprayed YSZ coatings were analyzed by scanning electron microscopy (SEM-LEO 438 VP, Carl Zeiss AG, Oberkochen, Germany). The SEM pictures were then processed by image analysis software (Image J, U.S. National Institutes of Health, Bethesda, MD, USA) to measure the percentage of molten and semi-molten areas embedded in coating microstructure, and the distribution of the nanostructured areas. The size of the regions used for porosity measurements was 350 x 250 μm^2.

2.3 Mechanical properties

The mechanical properties of YSZ coatings were determined by Micro and Nano Indentation tests. A measuring system of CSM Instruments SA, Peseux, Switzerland, equipped with three objective lenses (with magnitude of 5x, 20x and 100x) and a ConScan, was used.

In order to perform Indentation tests the cross sections of the first set of coated samples were prepared using standard metallographic procedure for ceramic coatings, including low-speed sectioning, cold mounting in vacuum in two-part epoxy resin, grinding, polishing and finishing to 0.25 μm.

The indentations were performed on a portion of the ceramic top coat containing areas with different melting degree and were equally spaced (40 μm for NI and 60 μm for MI) in order to avoid the mutual influence of consecutive indentations [15]. Due to the presence of microstructural defects such as pores and poorly compacted areas, an Adjust Depth Offset operation was set every ten indentations in order to find the height position of the sample surface (acronym ADO in Fig. 1). NI tests were performed according to a 4x10 matrix (with lines parallel to the substrate) by using a Berkovich tip, a loading and unloading speed of 3 mN/s, a hold time of 10 s and two different values for the maximum load: 8 and 100 mN. MIs, distributed according to a 3x10 matrix, were also

performed by using a Vickers microindenter with maximum loads of 50 gf and 100 gf and a hold time of 10 s.

The values of reduced Young's modulus Er and hardness H were obtained by load-depth curves, according to Oliver and Pharr theory [16,17], and then the experimental data were analyzed by assuming a two-parameters Weibull statistical distribution [18].

2.4 Tribological properties

The second set of specimens was addressed to wear tests. For the tribological characterization ball-on-disk tests were carried out using a CSM Instrument Tribometer. The tests were performed in dry mode with a sintered α-Al_2O_3 ball (6 mm in diameter), a wear track radius of 5 mm, a normal load of 10 N, a linear speed of 0.1 m/s and a cycle number of 20,000. The wear rate was calculated according to the formula (1):

$$WR = \frac{V}{F\,l} \qquad (1)$$

where *WR* is the wear rate [mm^3/(Nm)], *V* is the worn volume [mm^3], *F* is the normal applied load [N] and *l* the sliding distance [m]. The track profile was determined by means of a Taylor-Hobson Surtronic 25 profilometer (Rand Taylor Hobson Ltd., Leicester, UK) and as the maximum depth of the worn area exceeded the full scale of the profilometer (300 μm) the CSM Instrument ConScan was used. Ten randomly located profile measurements were performed on each tested sample after removing wear scraps by an air jet. The wear tracks were finally analyzed by scanning electron microscopy.

3. Results and Discussion

3.1 Microstructure

X-ray diffraction patterns of YSZ powder and coatings produced using different processing parameters are shown in Fig. 2: the high-angle (72-75°) region of the diffraction patterns showing (400) zirconia reflections is drawn. The powder feedstock is mainly composed of tetragonal t zirconia phase with smaller amounts of cubic and monoclinic zirconia phases, according to Joint Committee on Powder Diffraction Standards (JCPDS) available at International Centre for Diffraction Data (no. 81-1544 for tetragonal, no. 49-1642 for cubic and no. 37-1484 for monoclinic zirconia). All the coatings are composed of a mixture of metastable t' zirconia phase and tetragonal t phase. The metastable t' phase is associated to the molten part of the powder agglomerated particles, whereas the tetragonal t phase is associated to their retained nanostructured unmelted nanostructured part. No monoclinic phase was detected in the coatings. The calculation of the percentage of t' and t zirconia phases cannot be properly performed by XRD spectra because of the overlapping between the related peaks. As reported below, more reliable estimation can be obtained by studying the distribution of retained nanostructured areas in the coating microstructure using scanning electron microscopy.

Figure 3 shows the cross sectional SEM microstructure of nanostructured YSZ coatings produced at the spraying distance of 80 mm and using different values of plasma current (500, 565 and 630 A). The plasma current is proportional to the plasma power and to the temperature of the sprayed particles, so that it can be used to have a good control on the degree of melting of the particle agglomerates. All the coatings exhibited a bimodal microstructure composed of well melted splats (dark grey dense areas in the pictures) and partially melted nanostructured areas (light grey areas) possessing an intrinsic porosity derived from their pre-agglomeration, as shown in Fig. 4 (a). The nanostructured areas are composed of loosely bound nanostructured particles.

Figure 4 (b) shows the morphology of the related powder particles, so that it can be deduced that the nanostructured zones retained in the final coatings were not affected by complete melting during

processing. The inset shows some clusters of nanograined particles with size close to 100 nm. During processing the hot plasma gas penetrated inside the agglomerated particles of the powder feedstock, melting their surface, while their core remained unmelted. The low heat transfer associated to their intrinsic porosity, the short residence time of the same sprayed particles in the plasma jet and the high quenching rate of the solidified splats at the substrate surface were able to reduce the mechanism of grain growth and nucleation, thus preserving great part of the starting nanostructure in the final coating.

As well displayed in Fig. 3, the well melted areas cement the loose microstructure, providing good mechanical integrity. The distribution of the nanostructured areas is more uniform for lower values of plasma current. For increasing values of this parameter the melting degree of the powder particles enhances, thus leading to denser coating with lower content of nanostructured areas. The flight path and the temperature history of the agglomerated particles in the plasma jet affect their distribution in the final coatings. The melting process is strongly related to the temperature distribution in the plasma jet and to the heat transfer to the porous agglomerates.

Table I reports the amount of retained nanostructured areas measured by image analysis along the cross section of nanostructured YSZ coatings produced using different process parameters. At constant spraying distance the percentage of nanozones decreases with increasing the plasma current, due to the better melting of the particle agglomerates, so that denser coatings are produced. This effect is more pronounced at 80 mm. The effect of spraying distance is more pronounced at the lowest value of plasma current. Higher spraying distance involves higher residence time of the sprayed particles in the plasma jet, better melting and thus higher deposition efficiency and higher coating thickness.

It is worth noting that the percentage of nanostructured areas embedded in coating cross section can be properly optimized based on the application the coating is addressed to. High retention of nanozones (30-40%) is particularly desired for manufacturing of abradable coatings with relatively low mechanical integrity. These coatings can be used in turbine engines to minimize the bypass

flow of hot combustion or cold compressor gases through the spaces between the rotating blade tips and the walls of the shroud, in order to provide seal and improve the efficiency.

On the contrary, lower retention of nanostructures (20%) is preferable for development of thermal barrier coatings with low thermal conductivity, high structural integrity and resistance to the infiltration of oxygen and molten salts in severe working environments (stator turbine blades and vanes). The presence of nanostructured areas with low sintering rate can counteract the high-temperature densification of YSZ coatings, which negatively affects the compliance and the thermal property, thus retarding extended microcracking and TBC delamination [12].

Nanozones play a significant role on the thermal shock resistance and durability of TBCs, because they act as crack arresters in the case of microcracking promoted by thermal stresses produced by thermal expansion mismatch between overlapped layers, thus increasing the fracture toughness [12,19]. For this reason a Vickers indentation at very high load (5000 gf) was performed on one of the produced samples in order to induce cracks (white circles in Fig. 5). In the detailed micrograph taken at higher magnification it can be observed as cracks that propagate in the molten phase are arrested by nanozones.

Columnar grains with diameter in the range from 50 to 300 nm are detectable within coating microstructure (Fig. 6). They are oriented along the direction of the grain growth and derived from heterogeneous nucleation at splat boundary produced by the heat flow released by the crystallization of the previous deposited splats. Some equiaxed grains can be also observed at splat boundary. They are produced by homogeneous nucleation, occurring when the heat loss promoted by cooling at the substrate is higher than the heat released by the crystallization [19].

3.2 Mechanical properties

Tables II and III summarize the values of Young's modulus, nano and microhardness measured on the cross sections of nanostructured YSZ coatings, deposited at spraying distance of 80 and 100

mm, respectively, and using different values of plasma current parameter. The measured values magnitude is in good agreement with that of results in literature [20,21].

It should be noted that the mechanical properties tend to increase with increasing the plasma current and the spraying distance. Specifically, at constant spraying distance, for increasing values of current, an average increase of 9% and 30% for Er and 13% and 60% for H, was observed, from nanoscale to microscale, respectively. Instead, the influence of the spraying distance is less prominent. At constant current value, for increasing values of torch-substrate distance, an average increase of 4% and 7% for Er and 3% and 34% for H was recorded, from nanoscale to microscale. It should also be noted that the values of the mechanical properties exhibited large scattering.

Figure 7 shows the load-depth (P-d) curves obtained by nanoindentations performed in the melted areas (continuous line) and in partially melted ones (dashed line), respectively. The curves refer to coatings produced at 500 A and 100 mm, but similar behavior was noticed for all the other samples. The parameters used for NI were: maximum load 100 mN, loading and unloading speed 3 mN/s, hold time 10 s.

It is possible to observe that in the melted phase lower maximum penetration was noticed (709 nm versus 2056 nm in the partially melted phase) as well as higher unloading curve slope. This suggests that the melted phase is characterized by higher stiffness and hardness in comparison with the partially melted area [16,17].

Indeed, as shown in Fig. 8, the size of the imprint is bigger in partially melted area. The nanostructured areas are characterized by porosity at nanoscale which reduces the cohesion between the agglomerated nanostructured particles. In addition, the curves in Fig. 9 show that the melted phase reveals a weak creep phenomenon, whereas the unmelted one is quite affected by it: in fact, it presents a great depth increase during the hold time at the maximum load. Based on the observations herein reported, one can conclude that the increase of the mechanical properties, observed in Tables II and III, is related to the increase of the melted fraction in YSZ coatings when higher values of current and distance are employed (Table I).

The usage of increasing current values involves higher plasma power, higher temperature of the sprayed particles and therefore lower retention of nanostructured areas and higher coating density. As previously reported, higher distance involves higher residence time of the sprayed particles in the plasma jet and better degree of melting, even if the effect of distance on the experimental trend of the mechanical properties was not always consistent, probably because of a kind of mutual influence with current. This aspect could be analyzed in future works by performing an experimental plan that provide a third level of torch-substrate distance and more in-depth analysis. As clearly observed in Tables II and III, the values of the mechanical properties measured at microscale are lower than those obtained at nanoscale, because of the larger analyzed volume and the higher influence of typical defects embedded in coating microstructure, such as coarse pores, splat boundaries and microcracks.

Moreover, for each indentation technique employed, as the indentation load rises the analyzed volume grows and the same microstructural defects become more significant, enough to bring down the mechanical properties, that result always more averaged and far from those of bulk stabilized zirconia [14,15].

Further analysis showed that the mechanical properties don't change across coating thickness and their variation is so small to be covered by the high scattering of the results (related to the different characteristics between melted and partially melted phases). In order to understand the reasons of this high scattering, two series of NIs were performed on the areas with different morphology, by using a maximum load of 8 mN and a time for loading and unloading of 10 s, without any hold time. Figure 9 shows some of the load-depth curves obtained.

It is interesting to notice that the curves related to the melted area (continuous lines) are very close and repeatable, whereas the curves acquired during indentation in the unmelted area (dashed lines) are somewhat different and scattered. The well melted area is, in fact, characterized by lower scattering in the mechanical properties, whereas the second one exhibits widely scattered data

(Table IV), typical of structures produced by nanostructured agglomerates assembly and characterized by intrinsic porosity.

Table IV summarizes the mean values and the standard deviations of the elastic modulus and hardness for both these areas.

Figure 10 shows the distribution of Er and H, in a bilogarithmic scale [18], for the well melted and unmelted areas, by assuming a two parameters Weibull distribution for the mechanical properties. The data can be approximated with a linear regression curve. On the same graph, the values of shape and scale parameters are reported. According to the previous assertions, the melted phase, characterized by less scattered data, presents greater values of *m*. The probability density functions of Er and H are plotted, respectively, in Figs. 11 (a) and (b), in grey for the melted area and in black for the partially melted one.

The sample obtained by merging the experimental data related to melted and unmelted areas can be considered like a coating with the 50% of the two phases. The analysis of the distributions concerning this kind of sample can be very useful for the prediction of the mechanical properties of any other nanostructured coating. For this purpose, in Fig. 12, Er and H Weibull plot of this simulated coating are shown, while Figs. 11 (a) and (b) show (dashed lines) the related probability density function (obtained as a weighted average of the probability density of the data referred to single zones). It can be noted that the points related to partially melted phase are so scattered that they contaminate the data of the second section, concerning the melted area, and go also beyond this region (in this example it is just a point). The slope of the mixed section (the second one) increases by decreasing the level of contamination. Despite the data merging, the bimodal behavior of the coating can be clearly observed, due to the change in the slope of the Weibull plot. In order to find the transition point between the two regions the R^2 statistics analysis can be used [14]. It should be noted that the presence of points above the mixed zone may generate incorrect interpretations of the data distribution, by suggesting, erroneously, the existence of a third phase, and then a trimodal

distribution. Figure 13 shows the trends of the mechanical properties for the coatings produced in this work and tested by Nano Indentation at 8 mN.

In all the cases a bimodal Weibull distribution can be noticed, as also observed in any previous works [14,20]. The zone in the graph characterized by lower values of H or Er reflects the mechanical behavior of the partially molten phase and it is characterized by lower slope, owing to greater scattering, whereas the second one is characteristic of the mixed area. It is interesting to notice that, at constant torch-substrate distance, as current value rises the slope of the second regression line increases: this is caused by the increase of the degree of melting of the sprayed particles which results in lower probability of contamination of the data pertaining to the molten zone. Note that, at constant current level, the increase of the torch-substrate distance produces different trend, but the results are in good agreement with the volume fractions of nanostructured areas listed in Table I.

The results obtained by NI tests performed at maximum load of 100 mN showed similar behavior, but less noticeable changes in slope between the interpolating sections were detected. This effect is the consequence of the greater size of the volume involved during NI at higher load, which mediates the local properties and makes the bimodality of the distributions more difficult to be observed.

In turn the results obtained by Micro Indentation for the coatings produced at 500 A and 100 mm are shown in Fig. 14. The second region of the distributions of MI data exhibits lower slope with respect to the first one, unlike NI tests, and in agreement with the data reported in literature [14,20]. This behavior can be addressed to the scale effect for which microcracks and globular pores embedded in the molten areas are responsible of data scattering, since higher volume of material was under analysis [14].

Therefore at higher indentation loads the data distribution is almost single-mode, as shown in Fig. 14 (b). Similar behaviors was observed for the other five specimens produced with different values of current and torch-substrate distance.

3.3 Tribological properties

Figure 15 shows result about wear rate of the second set of samples tested by the ball-on-disk test. By comparing the wear behavior of nanostructured coatings to that of a conventional one (characterized by the same initial roughness of about 8 μm and tested with the same parameters listed in section 2.4) it can be noted that just the sample with the lowest nanozones percentage (20%) has a higher wear resistance and that the wear rate increases with increasing the values of nanozones percentage (values in Table I). For specimens with 31% and 36% of nanozones the coating was completely worn until the appearance of the superalloy substrate during the test.

Many researchers have reported superior wear performances for nanostructured ceramic coatings when compared to that of conventional coatings [12]. In this kind of coatings in fact the wear mechanism is a combination of brittle fracture and abrasive wear (promoted by delamination and detachment of small fragments or particles from the surface) and the presence of dense nanozones limits both of these phenomena. The brittle fracture is confined by the crack arrest effect whereas the abrasive wear is reduced by the wear scars of the nanostructured coating that are finer and smoother than those of the conventional coatings and form an adherent layer which limits wear [22].

These anti-wear performances refer to coatings with relatively low nanozones percentage (less than about 20%). When the amount of nanozones is higher (as observed for the samples analyzed in this work) the molten part of the semi-molten agglomerates can't fully infiltrate into the capillaries of their non-molten core during thermal spraying by causing the formation of porous and friable nanozones, typical of abradable coatings [12].

Therefore by varying process parameters the percentage of retained nanozones can be controlled in order to produce abradable coatings with different wear degrees or thermal barrier coatings with higher mechanical integrity.

Figure 16 shows the wear tracks of the three samples produced at torch-substrate distance of 100 mm and using different current values. It can be observed that the track becomes more pronounced

with decreasing the values of the current and increasing the percentage of retained nanozones. The dark zone in the middle of the track in Fig. 16 c) represents the metallic substrate by confirming the results showed in Fig. 15. The morphology of the wear area is the same for all the nanostructured coatings produced and it is shown in Fig. 17. In the magnification of Fig. 17 (b) the white holes highlight the cracks caused in the molten zones during the wear test that indicate the occurrence of a brittle fracture. However, the observed cracks are very few and the dominant wear mechanism of the analyzed nanostructured coatings, characterized by a high percentage of friable nanozones, comes from abrasive wear. Indeed, the darker areas in the worn zone (observable in Fig. 16 and Fig. 17) may represent not only the molten zones, but also the compaction of the fine debris produced during the wear test.

4. Conclusion

In this work the influence of some process parameters (plasma current and stand-off distance) on the microstructural, mechanical and tribological properties of plasma sprayed nanostructured YSZ coatings was investigated. The partial melting of the nanostructured particle agglomerates produced the formation of a bimodal microstructure composed of well melted splats and semimolten areas. Columnar and equiaxed grains were observed in the melted splats, while the partially melted areas did not suffer grain growth and retained porosity at nanoscale. An increase of plasma current promoted the increase of the particle temperature, improving the melting degree and the density of the coatings.

The reduction of the retained nanostructured areas produced significant increases of Young's modulus, hardness and wear resistance. The effect of the torch-substrate distance was more significant at lower current values.

The Nano and Micro Indentation tests, performed at various loads, in conjunction with Weibull statistical approach, revealed that the bimodal microstructure involved a bimodal distribution of the

mechanical properties, which tended to disappear with increasing the indentation load. The elastic modulus and the hardness decreased with increasing the indentation load, because of higher analyzed volume and stronger influence of the microstructural defects.

The ball-on-disk tests performed revealed that the nanostructured coatings produced with the APS process parameters set in this work were mostly abradable coatings characterized by wear rate higher than that of the conventional coatings, due to high presence of nanozones. The SEM images of the wear area showed that the morphology is the same for all the produced nanostructured coatings and that the dominant wear mechanism comes from abrasive wear rather than a brittle fracture.

The analysis of the influence of APS process parameters on coatings properties is really useful in order to engineer nanostructured YSZ coatings for different applications.

The development of a reliable procedure allowing a proper control of the percentage of the nanostructured areas embedded in coating microstructure is not easy to be achieved and will require a more detailed plan of experiments with the introduction of other process parameters and further investigations.

Acknowledgments

The nano- and micro-hardness measurements were performed with equipment kindly provided by "Centro Materiali, Tecnologie e Ricerca Avanzata (MaTeRiA)" from University of Calabria, funded with "Pon Ricerca e Competitività 2007/2013, Asse I Sostegno ai Mutamenti Strutturali Obiettivo Operativo 4.1.1.4, Potenziamento delle Strutture e delle Dotazioni Scientifiche e Tecnologiche, Azione I - Rafforzamento Strutturale".

The authors wish to thank C. Blasi for her valuable contribution coating manufacturing and P. Caliandro for preliminary SEM observations.

References

[1] J. A. Nesbitt, Thermal response of various thermal barrier coatings in a high heat flux rocket engine, Surf. Coat. Technol. 43/44 (1990) 458–469.

[2] N. Curry, N. Markocsan, X.A. Li, A. Tricoire, M. Dorfman, Next generation thermal barrier coatings for the gas turbine industry, J. Therm. Spray Technol. 20 (2011) 108-115.

[3] N.P. Padture, M. Gell, E.H. Jordan, Thermal barrier coatings for gas turbine engine applications, Science 296 (2002) 280-284.

[4] G. Di Girolamo, M. Alfano, L. Pagnotta, D. Sun, J. Zekonyte, R.J.K. Wood, On the Early Stage Isothermal Oxidation of APS CoNiCrAlY Coatings, J. Mater. Eng. Perf. 21 (2012) 1989-1997.

[5] X.Q. Cao, R. Vassen, S. Stöver, Ceramic materials for thermal barrier coatings, J. Eur. Ceram. Soc. 24 (2004) 1-10.

[6] G. Di Girolamo, L. Pagnotta, Thermally sprayed coatings for high temperature applications, Rec. Patent on Mater. Sci. 4 (2011) 173-190.

[7] J.R. Davis, Handbook of Thermal Spray Technology, ASM International, Materials Park, 2004.

[8] W.R. Chen, X. Wu, B.R. Marple, R.S. Lima, P.C. Patnaik., Pre-oxidation and TGO growth behavior of an air-plasma-sprayed thermal barrier coating, Surf. Coat. Technol. 202 (2008) 3787-3796.

[9] P. Puetz, X. Huang, R.S. Lima, Q. Yang, L. Zhao, Characterization of transient oxide formation on CoNiCrAlY after heat treatment in vacuum and air, Surf. Coat. Technol. 205 (2010) 647-657.

[10] M. Daroonparvar, M.A. Mat Yajid, N.M. Yusof, M.S. Hussain, Formation of a dense and continues Al_2O_3 layer in nano thermal barrier coating systems for suppression of the spinels growth on the Al_2O_3 oxide scale during oxidation, J. All. Comp. 571(2013) 205-220.

[11] M. Daroonparvar, M.A. Mat Yajid, N.M. Yusof, M.S. Hussain, Improved Thermally Grown Oxide Scale in Air Plasma Sprayed NiCrAlY/Nano-YSZ Coatings, J. Nanomater. http://dx.doi.org/10.1155/2013/520104.

[12] R.S. Lima, B.R. Marple, Thermal spray coatings engineered from nanostructured ceramic agglomerated powders for structural, thermal barrier and biomedical applications: a review, J. Therm. Spray Technol. 16 (2007) 40-63.

[13] J. Wu, H.B. Guo, L. Zhou, L. Wang, S.K. Gong, Microstructure and thermal properties of plasma sprayed thermal barrier coatings from nanostructured YSZ, J. Therm. Spray Technol. 19 (2010) 1186-1194.

[14] R.S. Lima, A. Kucuk, C.C. Berndt, Bimodal distribution of mechanical properties on plasma sprayed nanostructured partially stabilized zirconia, Mater. Sci. Eng. A 327 (2002) 224-232.

[15] A.C. Fisher-Cripps, Nanoindentation, 3rd edition, Springer, New York, 2011.

[16] W.C. Oliver, G.M. Pharr, An improved technique for determining hardness and elastic modulus using load and displacement sensing indentation experiments, J. Mater. Res. 7 (1992) 1564-1583.

[17] W.C. Oliver, G.M. Pharr, Measurement of hardness and elastic modulus by instrumented indentation: Advances in understanding and refinements to methodology, J. Mater. Res. 19 (2004) 3-20.

[18] W. Weibull, A statistical distribution function of wide applicability, J. Appl. Mech. 18 (1951) 293-297.

[19] G. Di Girolamo, F. Marra, C. Blasi, E. Serra, T. Valente, Microstructure, mechanical properties and thermal shock resistance of plasma sprayed nanostructured zirconia coatings, Ceram. Int. 37 (2011) 2711-2717.

[20] L. Wang, Y. Wang, X.G. Sun, J.Q. He, Z.Y. Pan, C.H. Wang, Microstructure and indentation mechanical properties of plasma sprayed nano-bimodal and conventional ZrO_2-8wt%Y_2O_3 thermal barrier coatings, Vacuum 86 (2012) 1174-1185.

[21] M. Saremi, A. Keyvanimahmoud, H. Sohi, Hot corrosion resistance and mechanical behavior of atmospheric plasma sprayed conventional and nanostructured zirconia coatings, Int. J. Modern Phys. Conf. Series 5 (2012) 720–727.

[22] B. Liang, G. Zhang, H.L. Liao, C. Coddet, C.X. Ding, Structure and tribological performance of nanostructured ZrO_2-3 mol% Y_2O_3 coatings deposited by air plasma spraying, J. Therm. Spray Technol. 19(6) (2010) 1163-1170.

Distance/current	500 A	565 A	630 A
80 mm	36 ± 4	23 ± 1	20 ± 4
100 mm	31 ± 2	25 ± 4	21 ± 1

Table I. Fractions (%) of retained nanostructured areas measured in YSZ coatings produced using different process parameters (plasma current and spraying distance).

Load	Current (A)	Er (GPa)	H (GPa)
8mN (NI)	500	151 ± 47	11.1 ± 5.4
	565	170 ± 33	11.8 ± 4,9
	630	174 ± 42	13.7 ± 4,8
100mN (NI)	500	100 ± 37	6.3 ± 3.9
	565	121 ± 37	8.3 ± 4.7
	630	125 ± 41	7.9 ± 4.3
50gf (MI)	500	76 ± 20	4.2 ± 2.4
	565	114 ± 28	6.1 ± 3.2
	630	123 ± 31	8.7 ± 5.0
100gf (MI)	500	80 ± 19	3.4 ± 1.4
	565	100 ± 26	4.4 ± 2.5
	630	125 ± 21	7.2 ± 2.7

Table II. Mean values and standard deviations of the mechanical properties for YSZ coatings sprayed at 80 mm and using different values of plasma current, measured by Micro and Nano Indentation tests using various loads.

Load	Current (A)	Er (GPa)	H (GPa)
8mN (NI)	500	159 ± 68	9.9 ± 5.8
	565	177 ± 54	11.7 ±5.1
	630	170 ±60	12.1 ± 6.2
100mN (NI)	500	108 ± 37	7.1 ± 4.3
	565	124 ± 53	9.1 ± 6.2
	630	135 ± 36	9.5 ± 4.0
50gf (MI)	500	78 ± 40	4.4 ± 3.3
	565	125 ± 40	10.3 ± 6.3
	630	158 ± 73	19.6 ± 12.9
100gf (MI)	500	76 ± 20	3.3 ± 1.9
	565	113 ± 29	5.9 ± 2.9
	630	109 ± 22	5.5 ± 2.6

Table III. Mean values and standard deviations of the mechanical properties for YSZ coatings sprayed at 100 mm and using different values of plasma current, measured by Micro and Nano Indentation tests using various loads.

Mechanical properties	Melted area	Unmelted area
E_r (GPa)	196 ± 29	131 ± 61
H (GPa)	15.8 ± 2.3	9.0 ± 7.8

Table IV. Elastic modulus and hardness of melted and unmelted phases.

Figure captions

Figure 1. Disposition of NI on the top coat cross section. Starting from the top: epoxy resin, top coat, bond coat and metallic substrate (magnitude 5x).

Figure 2. High-angle region of XRD spectra for YSZ (a) powder and coatings produced using different process parameters: (b) 500 A and 80 mm, (c) 500 A and 100 mm, (d) 565 A and 80 mm, (e) 565 A and 100 mm, (f) 630 A and 80 mm, (g) 630 A and 100 mm.

Figure 3. Cross sectional SEM microstructure of nanostructured YSZ coatings deposited at spraying distance of 80 mm and using various plasma current levels (a) 500 A, (b) 565 A and (c) 630 A.

Figure 4. (a) Cross sectional SEM microstructure showing the morphology of the retained nanostructured areas; (b) a view of agglomerated nanoparticles in the powder feedstock with detail of zirconia clusters.

Figure 5. Crack arrest produced by nanozones in plasma sprayed nanostructured YSZ coating.

Figure 6. Fractured coating cross section showing the morphology of the melted splats, composed of columnar and equiaxed grains.

Figure 7. Load-depth (P-d) curves corresponding to melted and partially melted phases.

Figure 8. Indent of NI (Berkovich) in (a) partially melted and (b) melted phase (magnitude 100x).

Figure 9. Load-depth (P-d) curves corresponding to melted and unmelted fractions and measured by NI at 8 mN.

Figure 10. Weibull plot of Er and H for melted and unmelted phases; the shape (m) and the scale (ϑ) parameters are also reported.

Figure 11. Probability density function of (a) Er and (b) H for melted (grey) and unmelted (black) phases and of the resultant bimodal distribution (dashed).

Figure 12. Weibull plot of H and Er data for the sample obtained by merging the data arising from melted and unmelted areas.

Figure 13. Weibull plot of H and Er for nanostructured YSZ coatings fabricated using different process parameters (plasma current and spraying distance) and tested by NI at 8 mN.

Figure 14. Weibull plot of H and Er for nanostructured YSZ coating produced at 500 A and 100 mm and tested by MI at (a) 50 gf and (b) 100 gf.

Figure 15. Wear rates of nanostructured YSZ coatings (produced with different process parameters and characterized by different percentages of nanozones (Table I)) and conventional YSZ coatings.

Figure 16. Wear tracks of samples produced with a distance of 100 mm and different current values: (a) 630 A (21% of nanozones); (b) 565 A (25% of nanozones); (c) 500 A (31% of nanozones).

Figure 17. (a) Wear zone morphology of the nanostructured coatings: the dashed curve represents the inner edge of the wear track; (b) magnification of the area in the white box of Fig. 17 (a).

Figure 1
Click here to download high resolution image

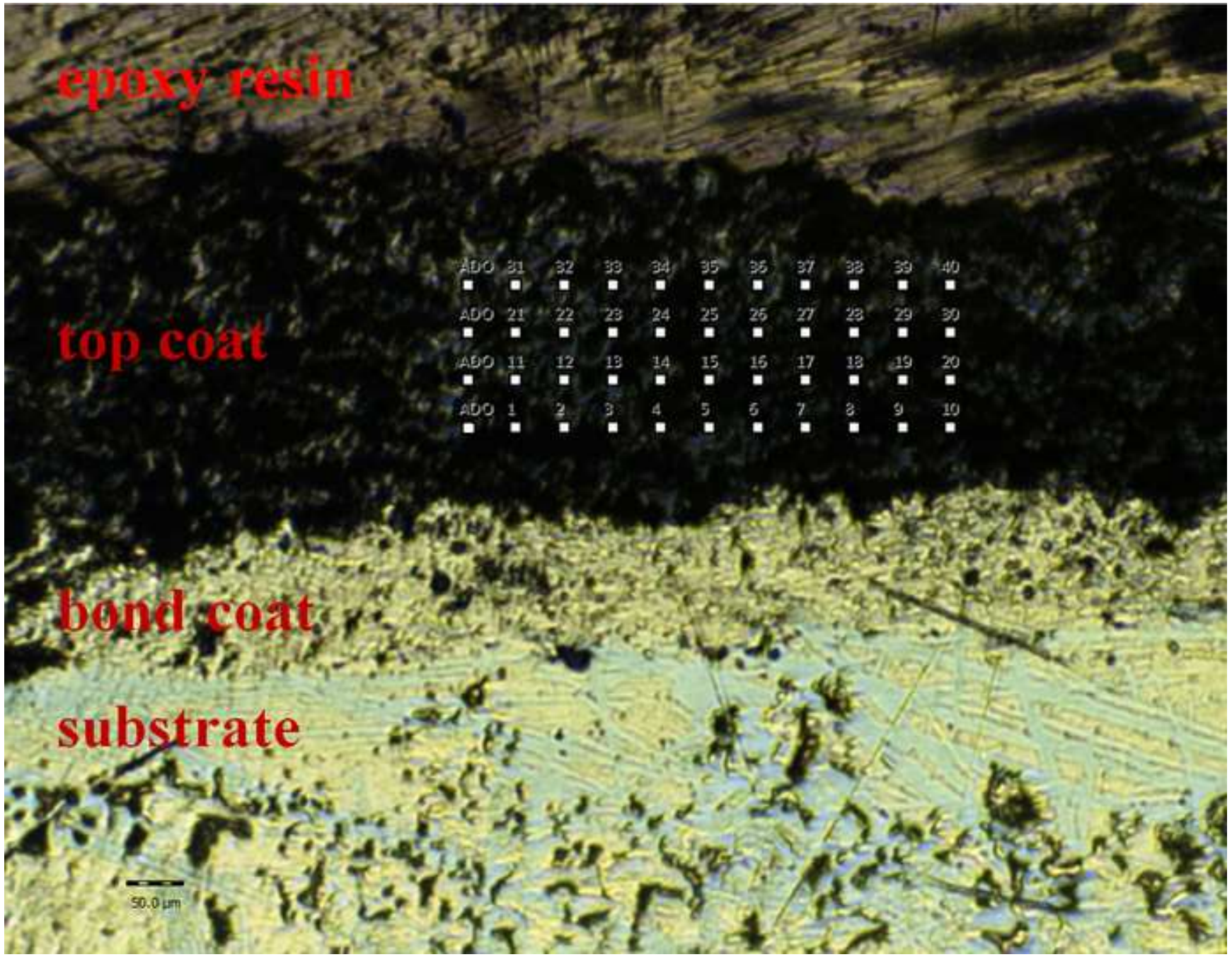

Figure 2
Click here to download high resolution image

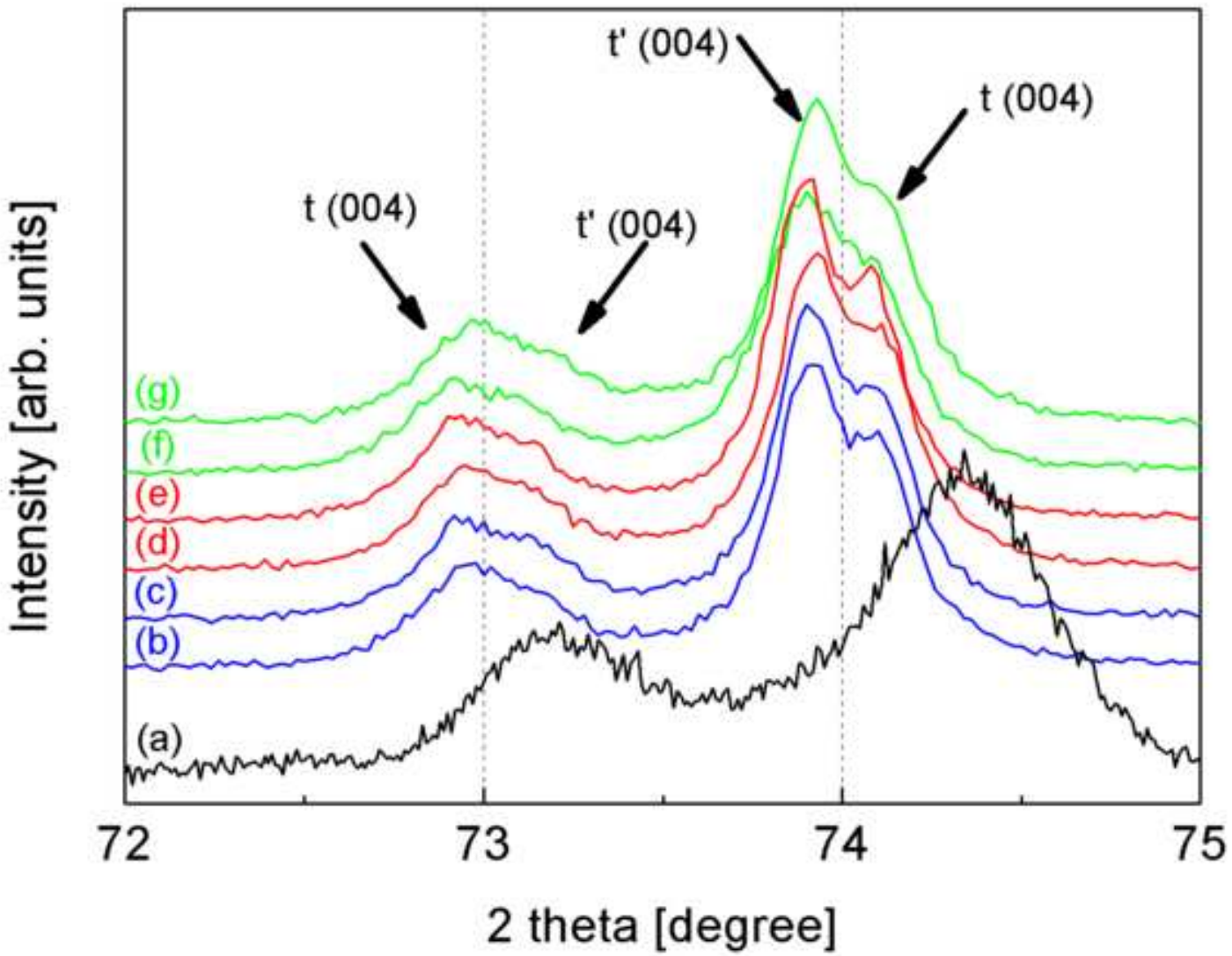

Figure 3
Click here to download high resolution image

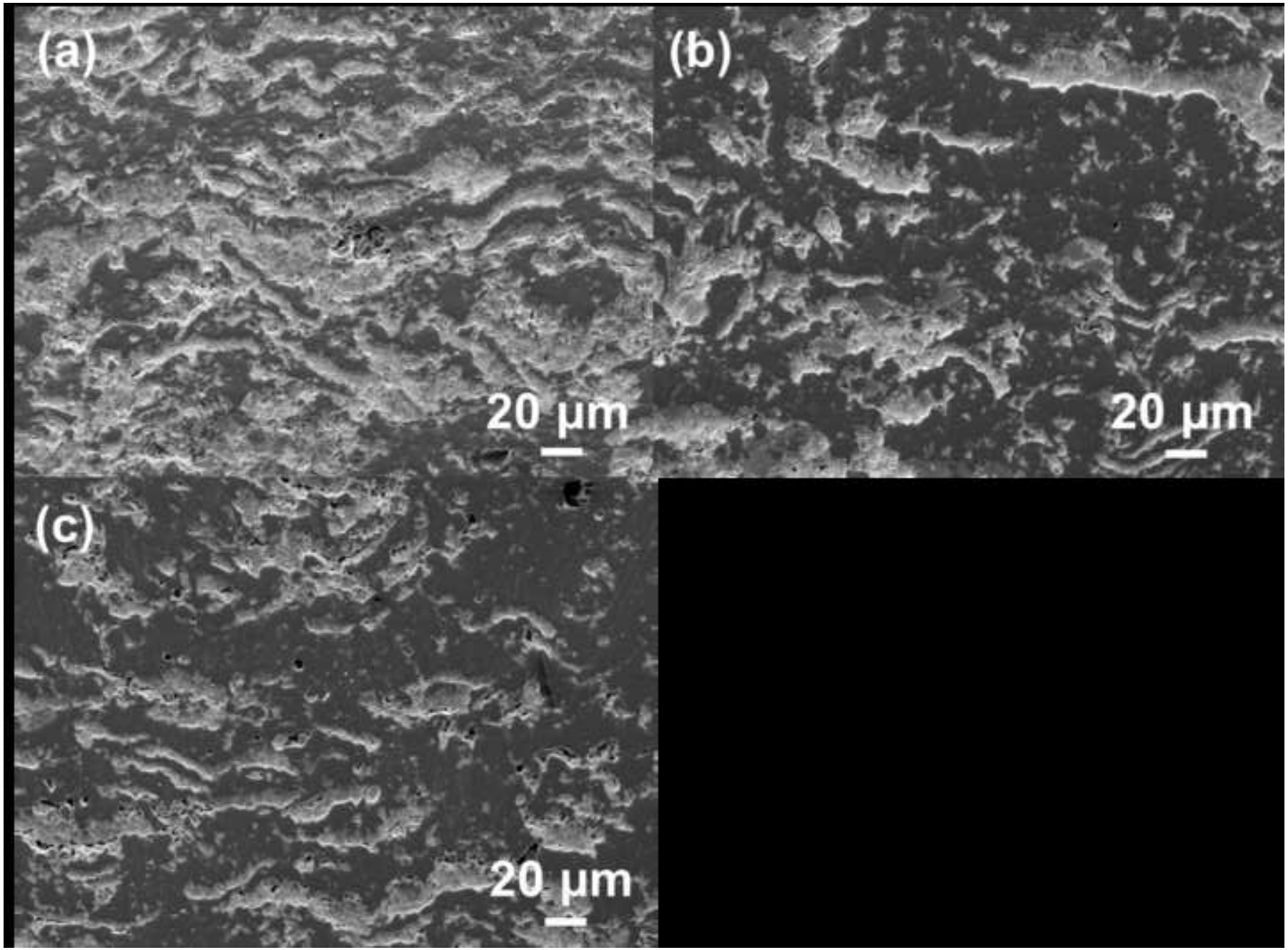

Figure 4(a)
Click here to download high resolution image

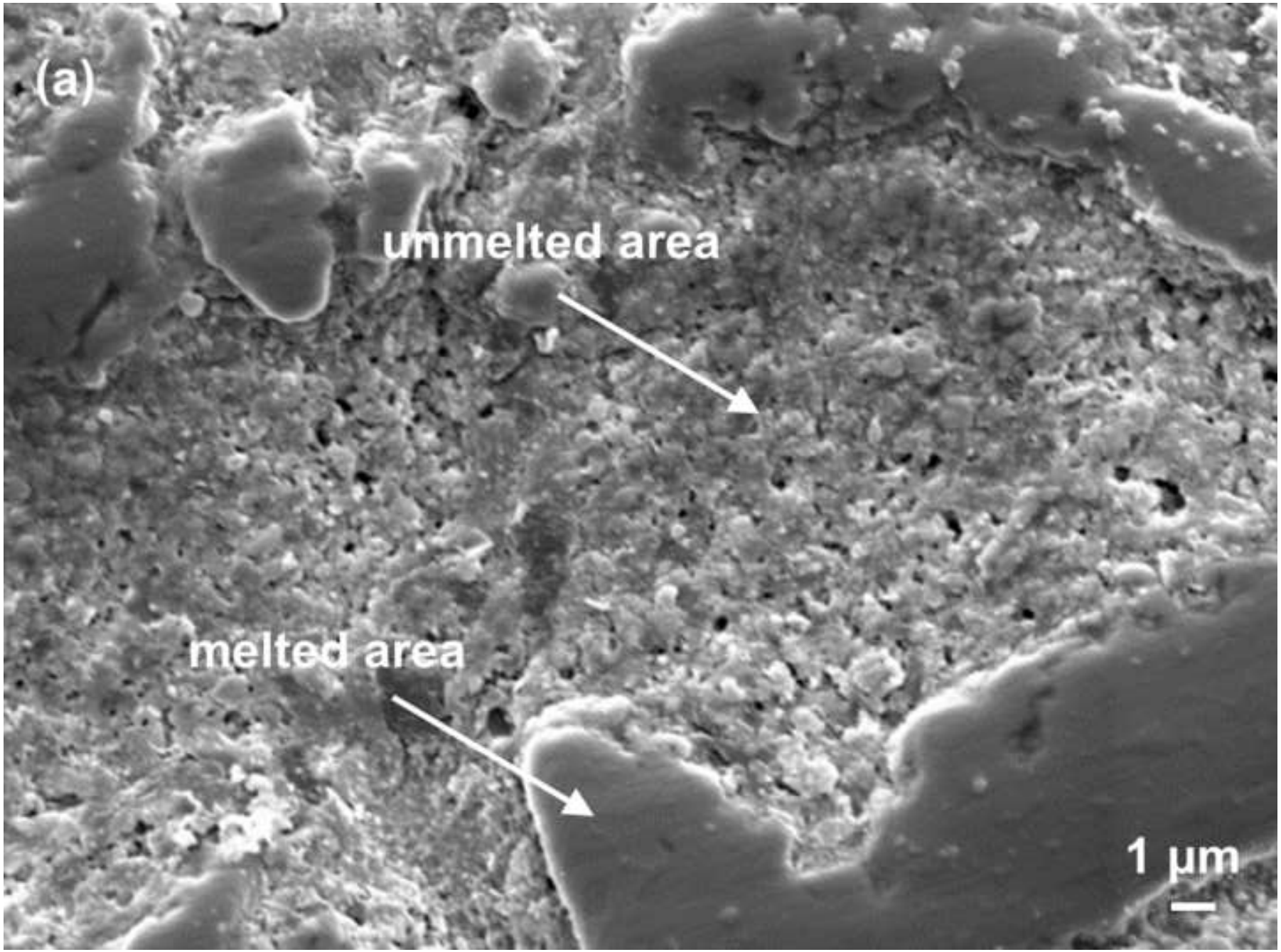

Figure 4(b)
Click here to download high resolution image

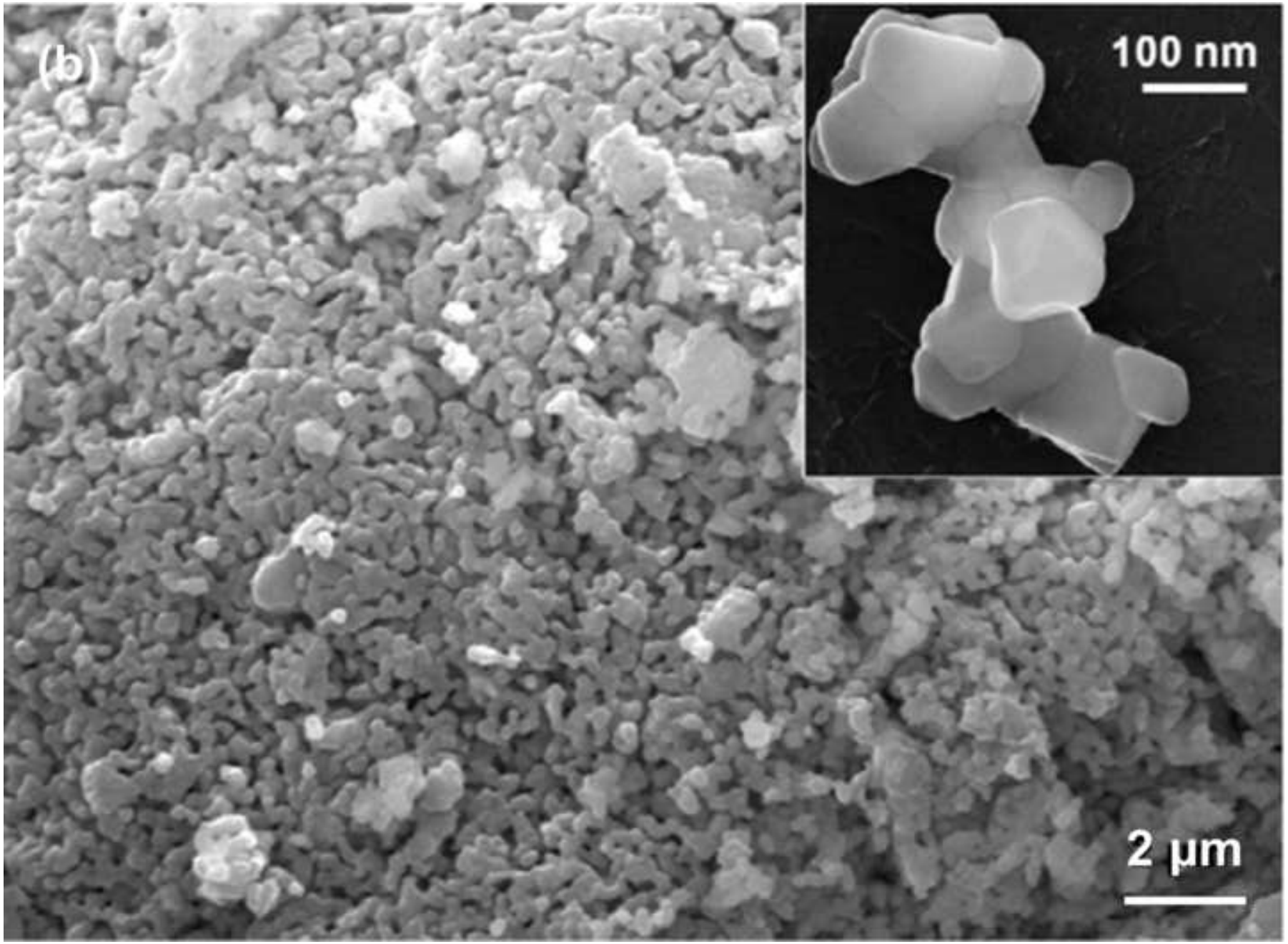

Figure 5
Click here to download high resolution image

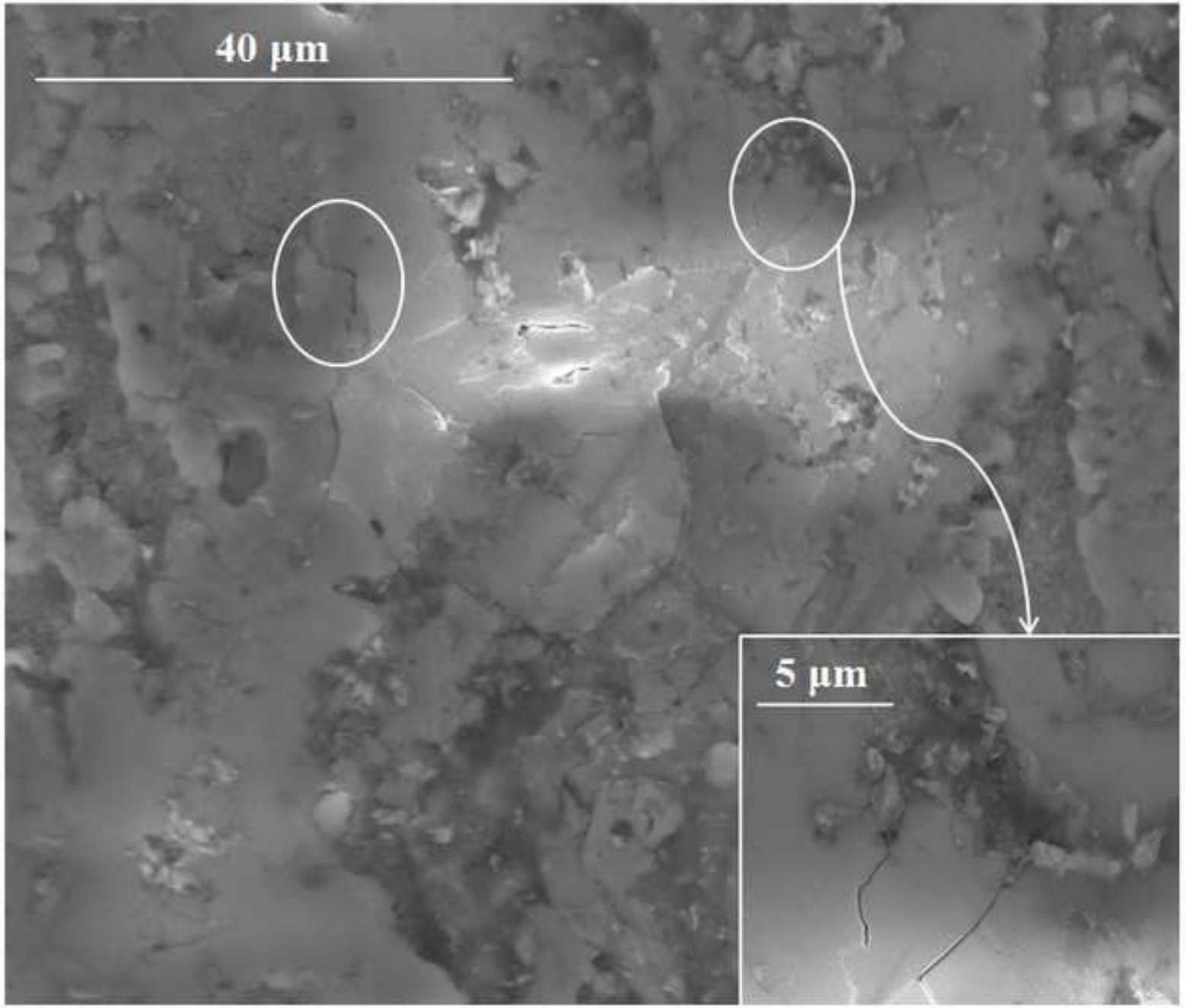

Figure 6
Click here to download high resolution image

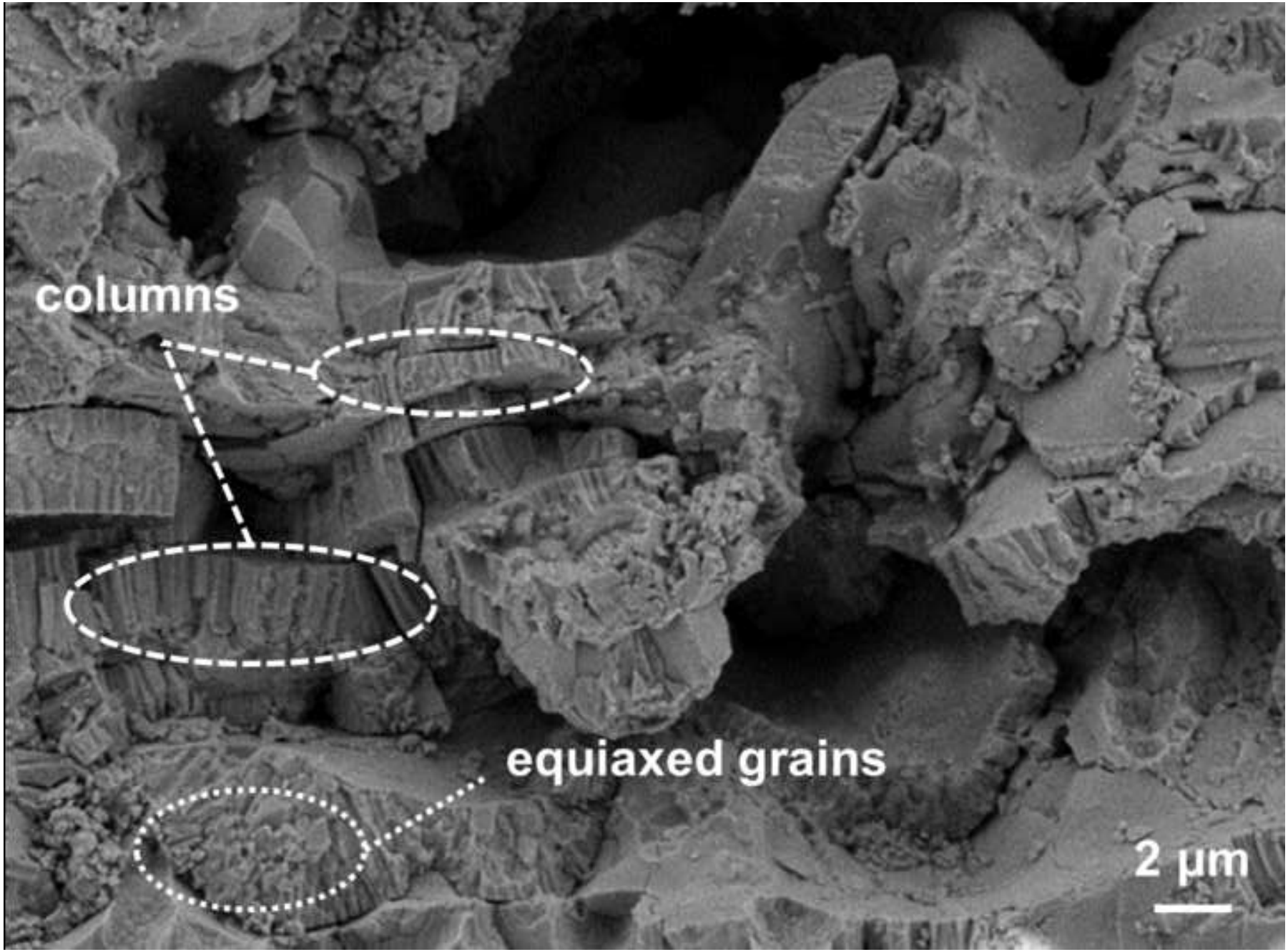

Figure 7
Click here to download high resolution image

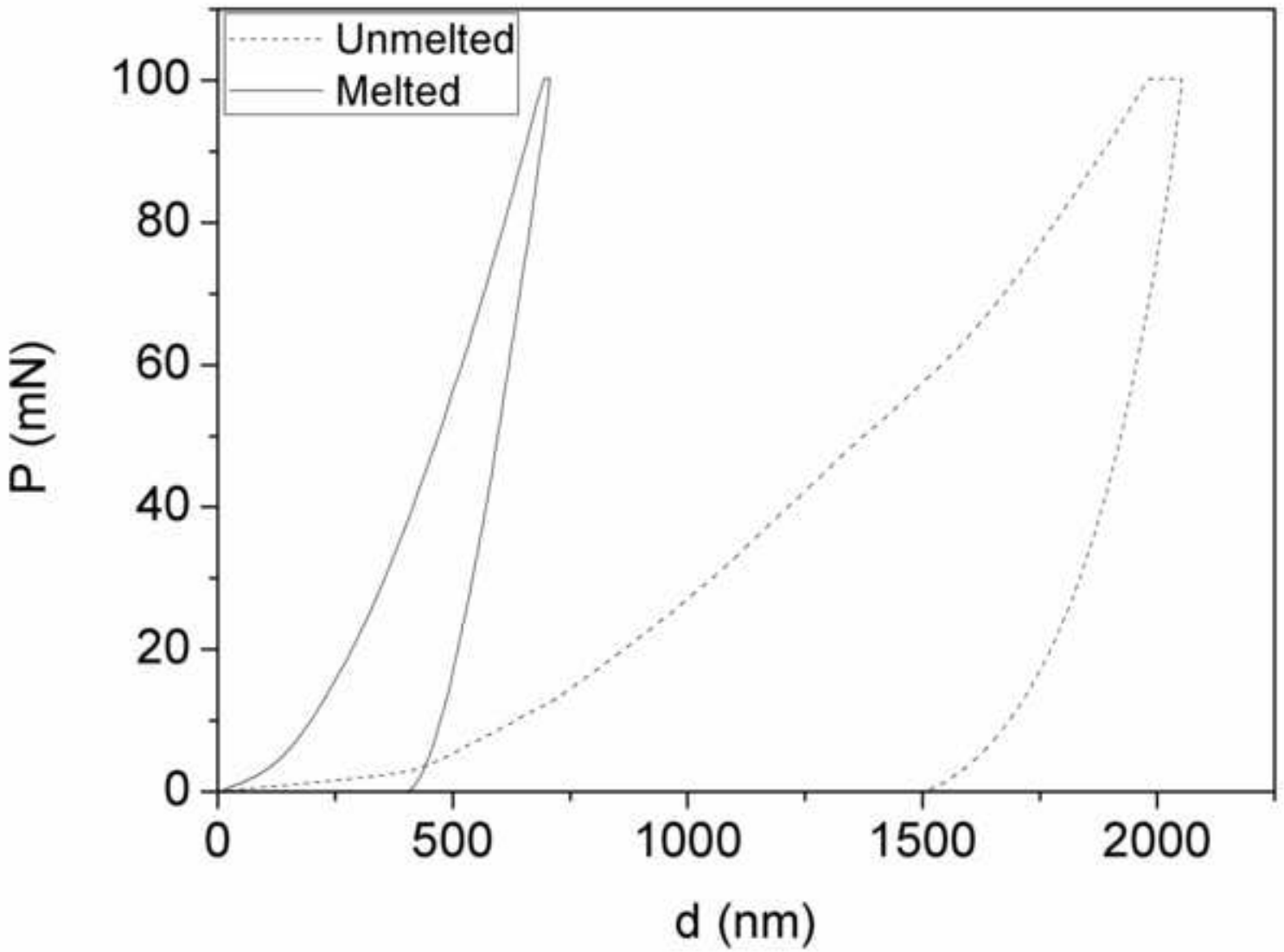

Figure 8(a)
Click here to download high resolution image

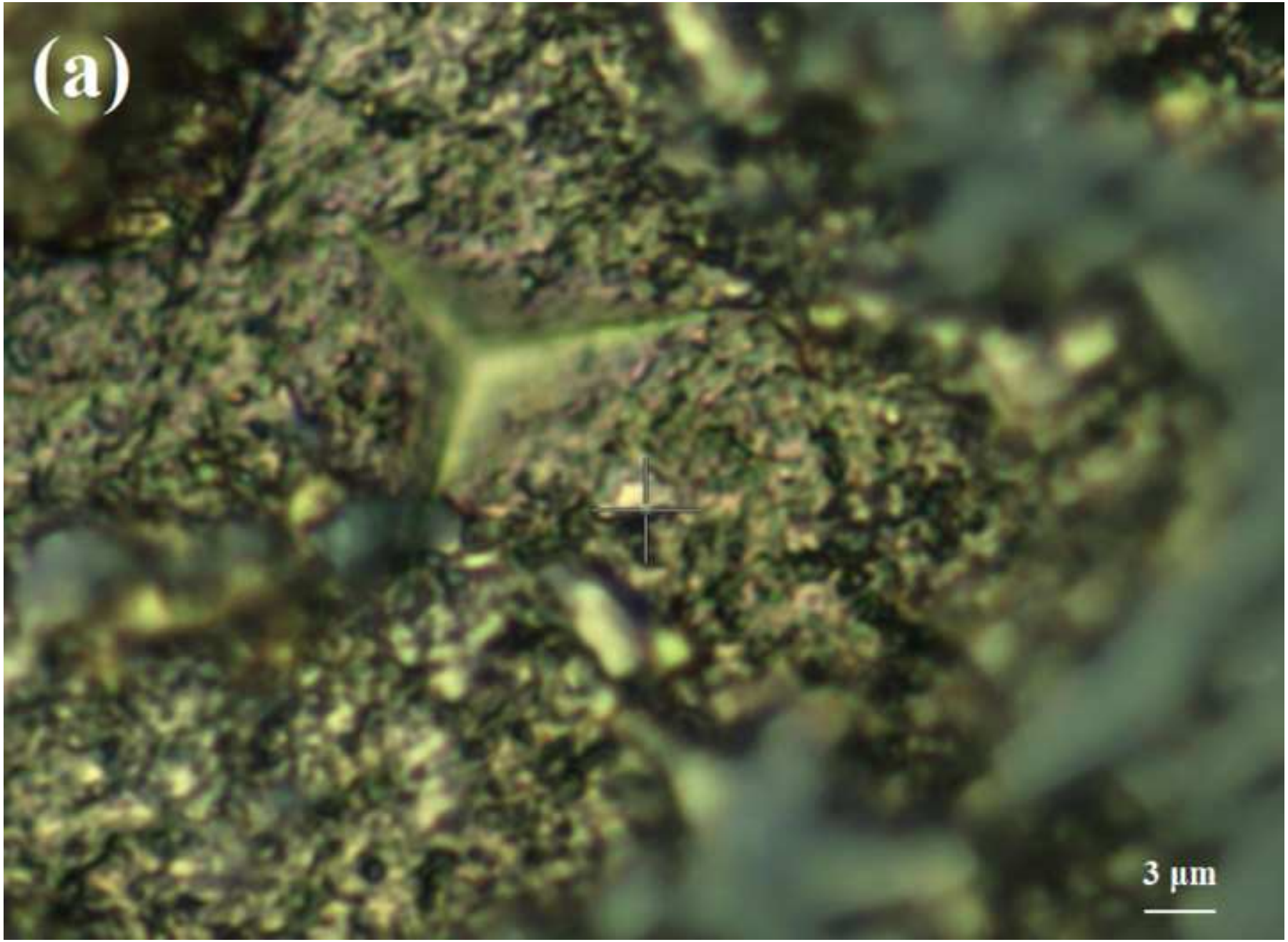

Figure 8(b)
Click here to download high resolution image

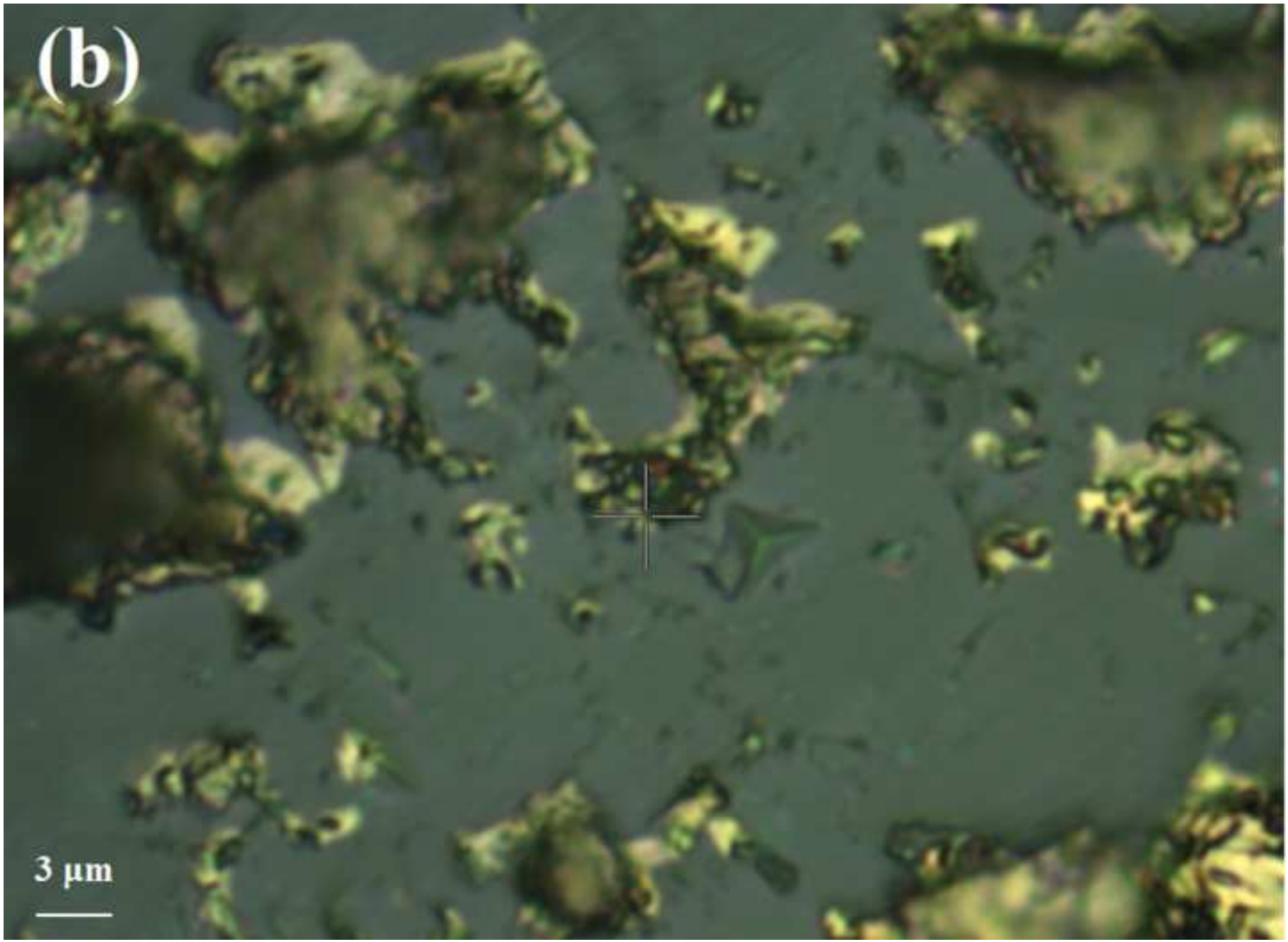

Figure 9
Click here to download high resolution image

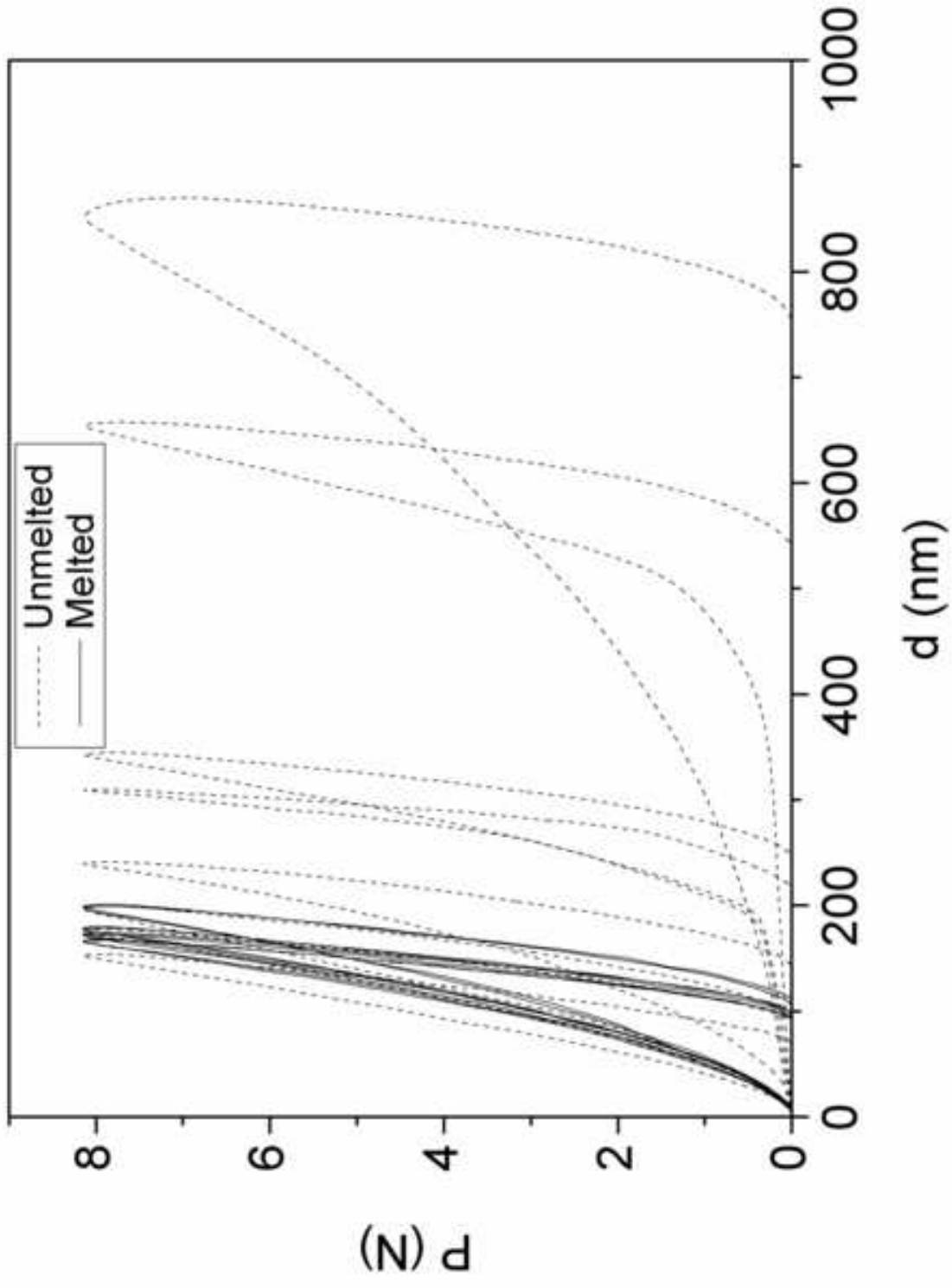

Figure 10
Click here to download high resolution image

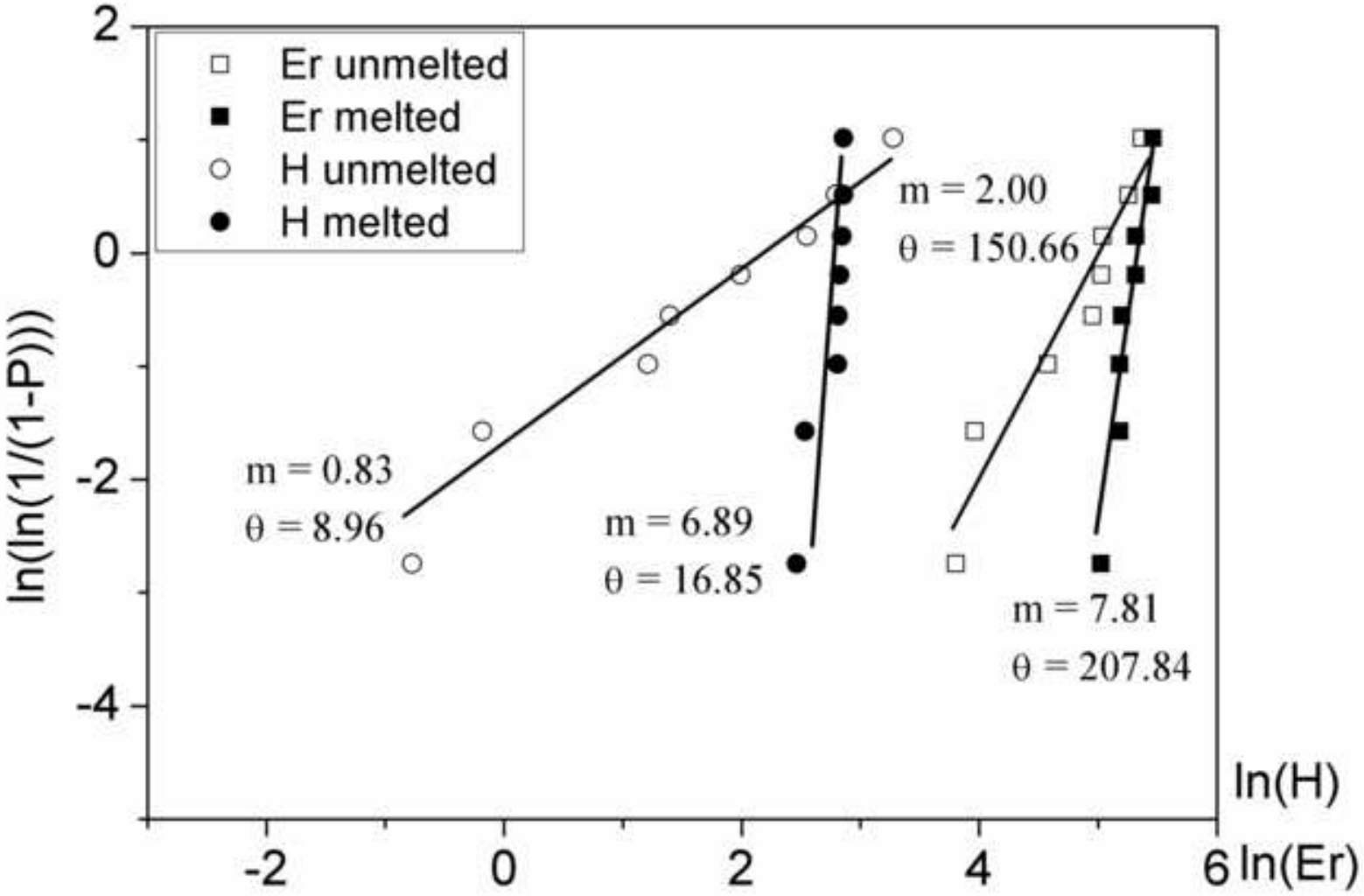

Figure 11(a)
Click here to download high resolution image

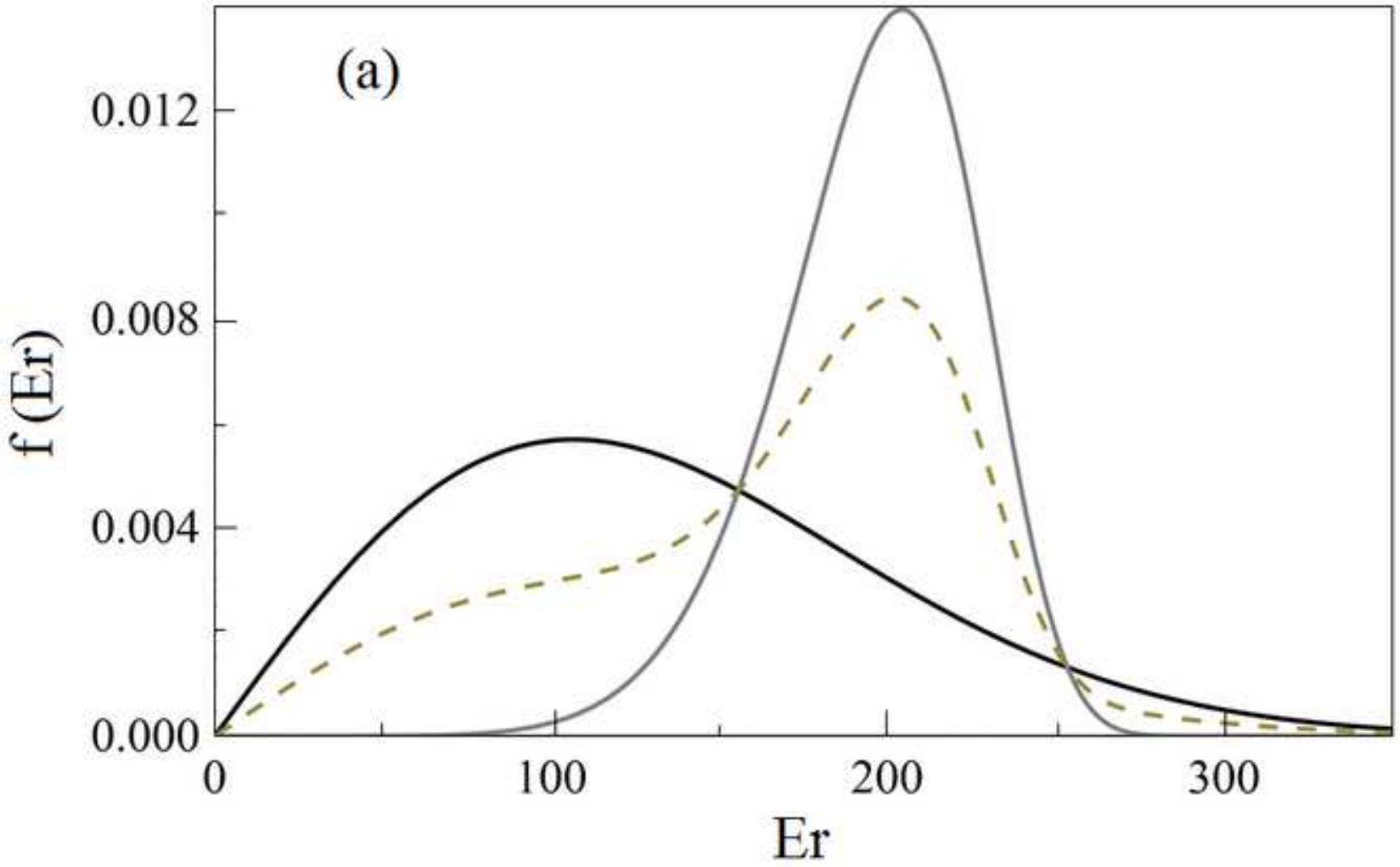

Figure 11(b)
Click here to download high resolution image

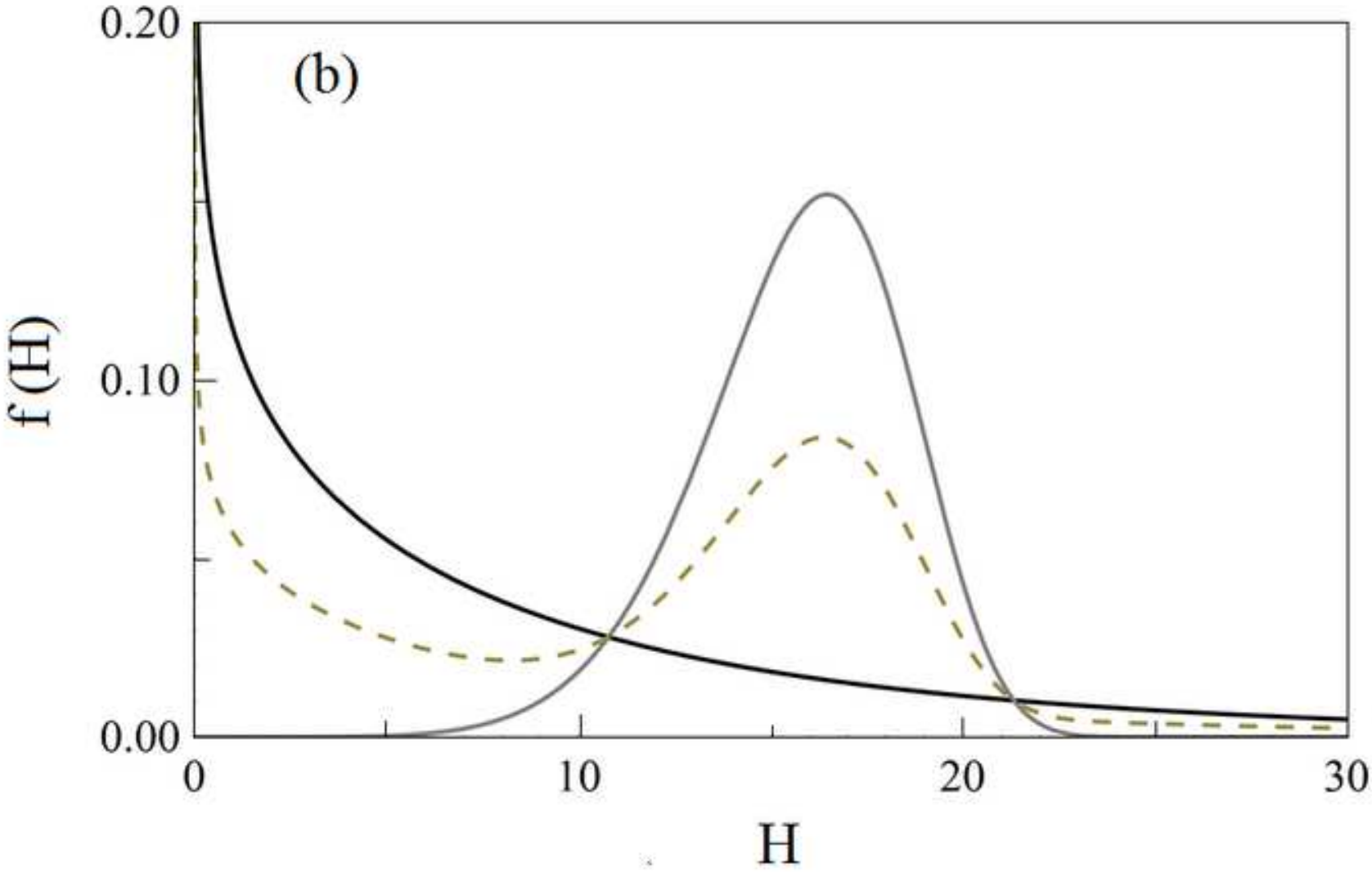

Figure 12
Click here to download high resolution image

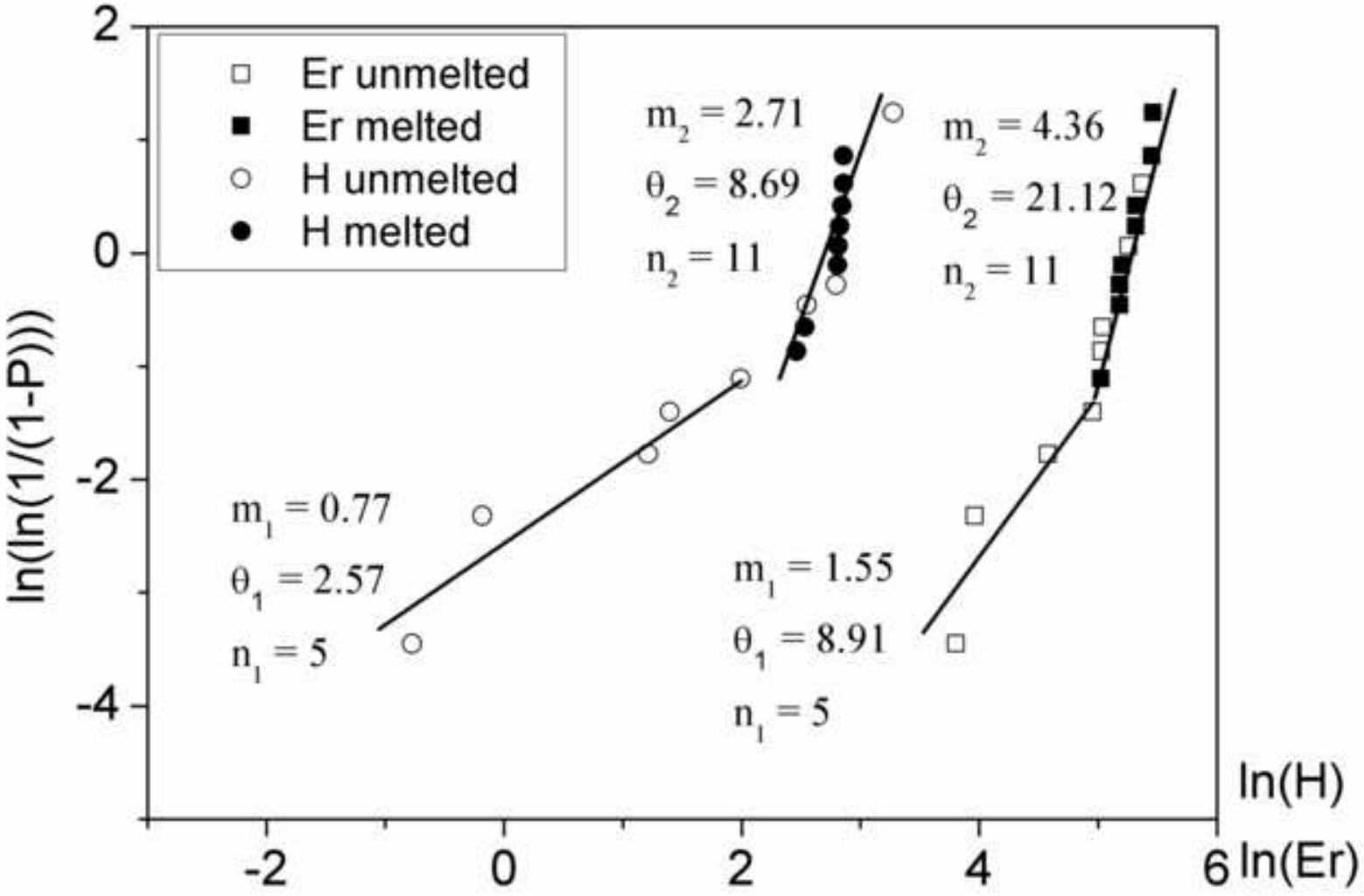

Figure 13(a)
Click here to download high resolution image

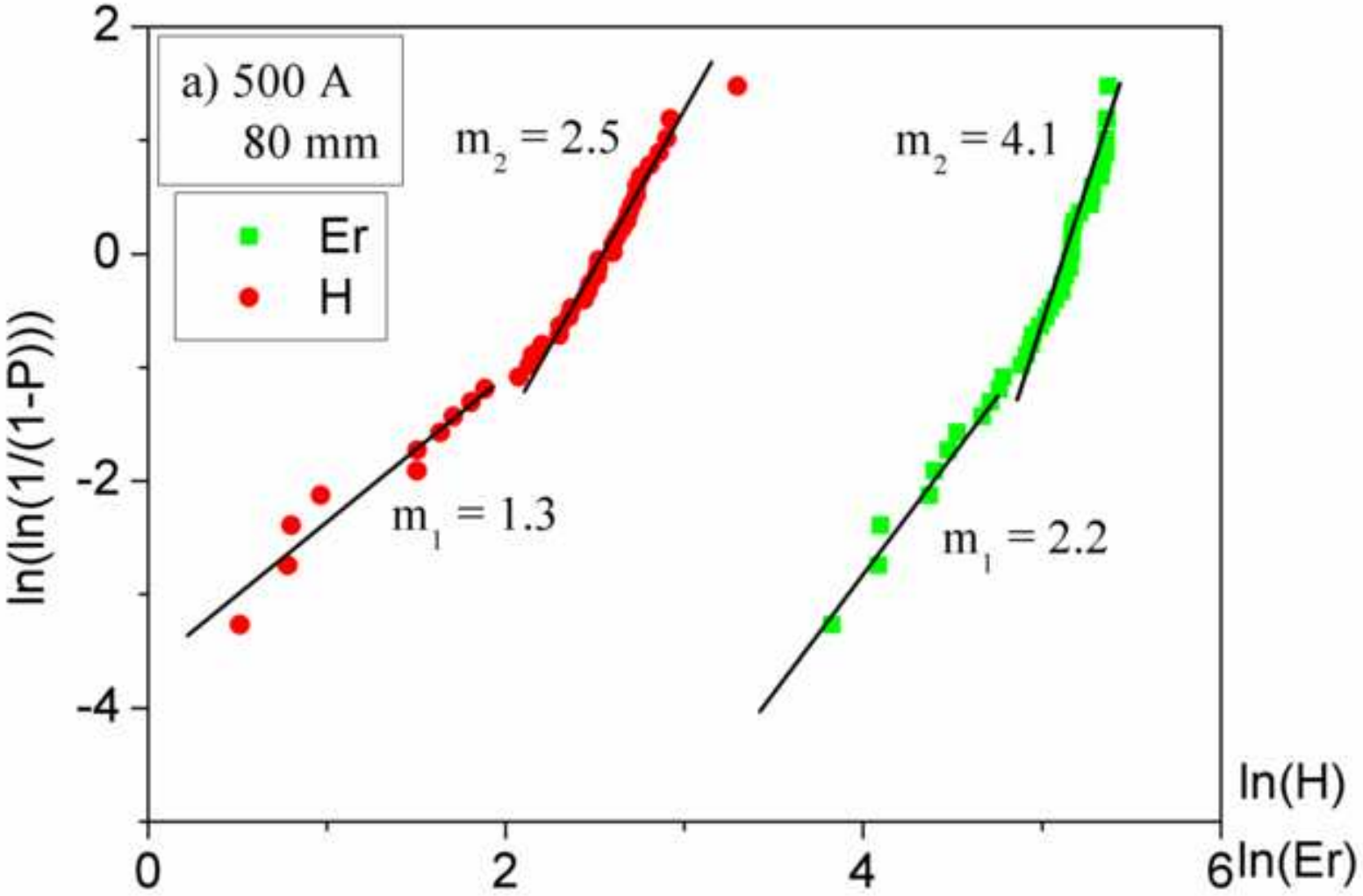

Figure 13(b)
Click here to download high resolution image

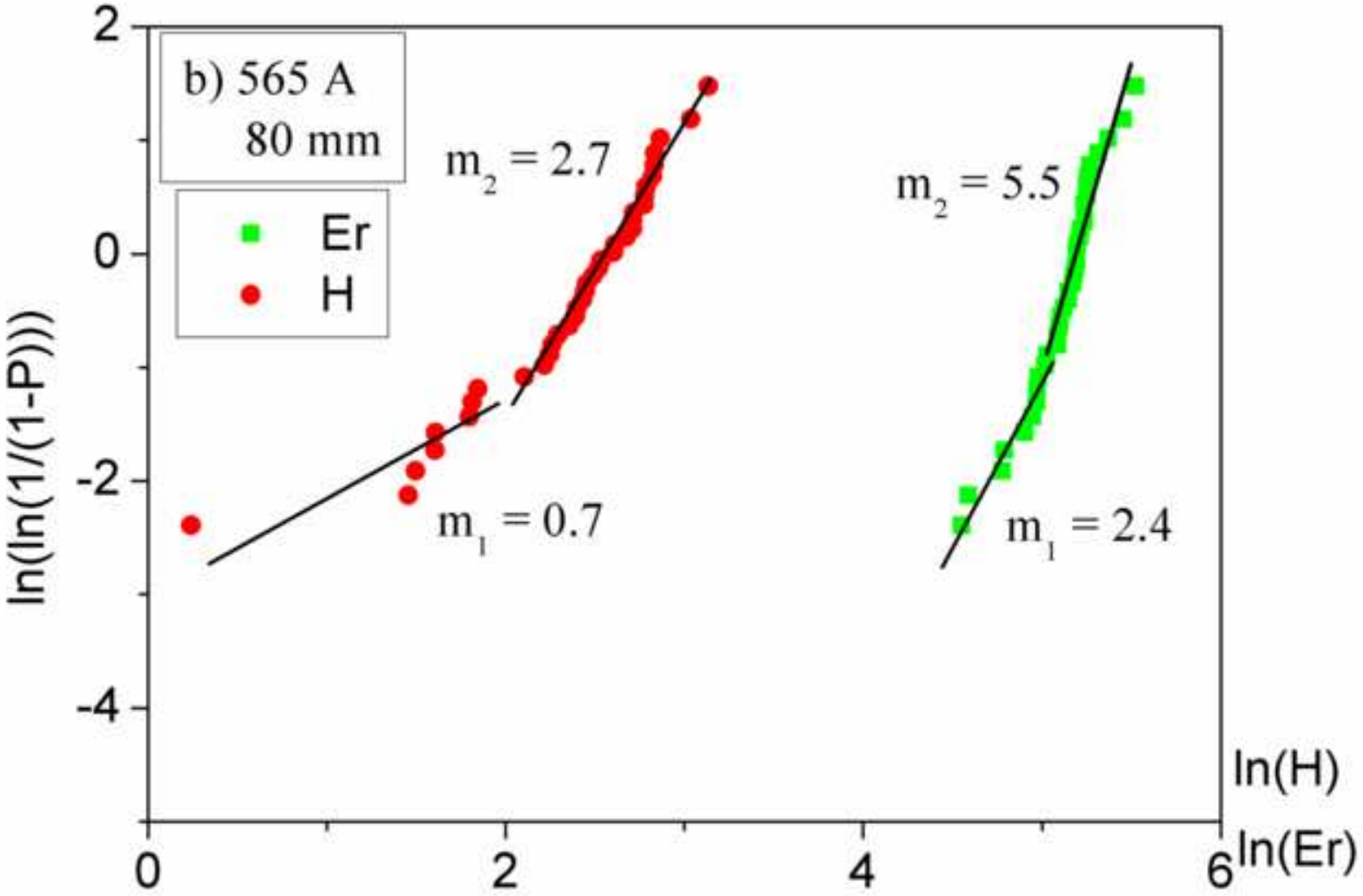

Figure 13(c)
Click here to download high resolution image

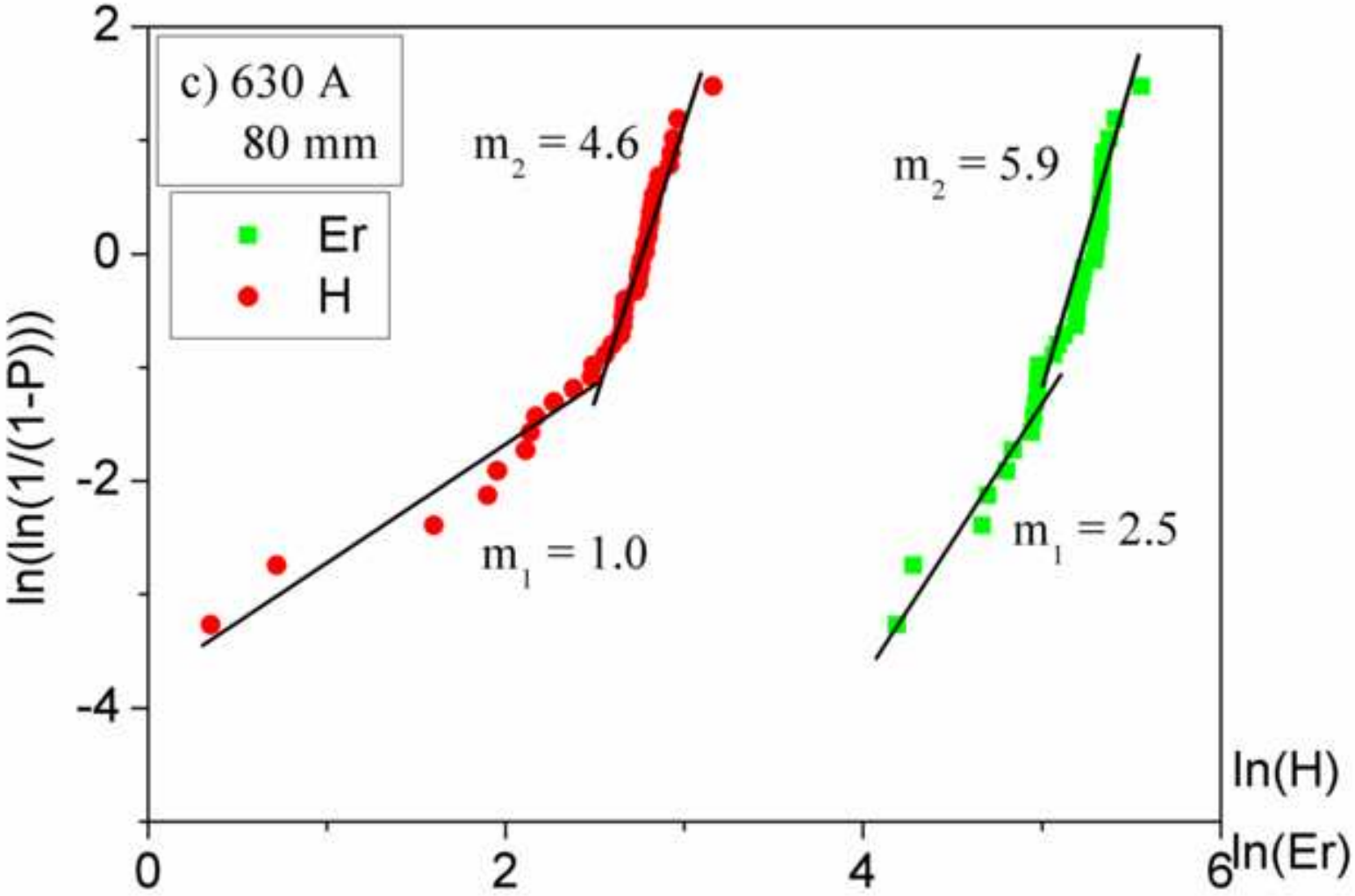

Figure 13(d)
Click here to download high resolution image

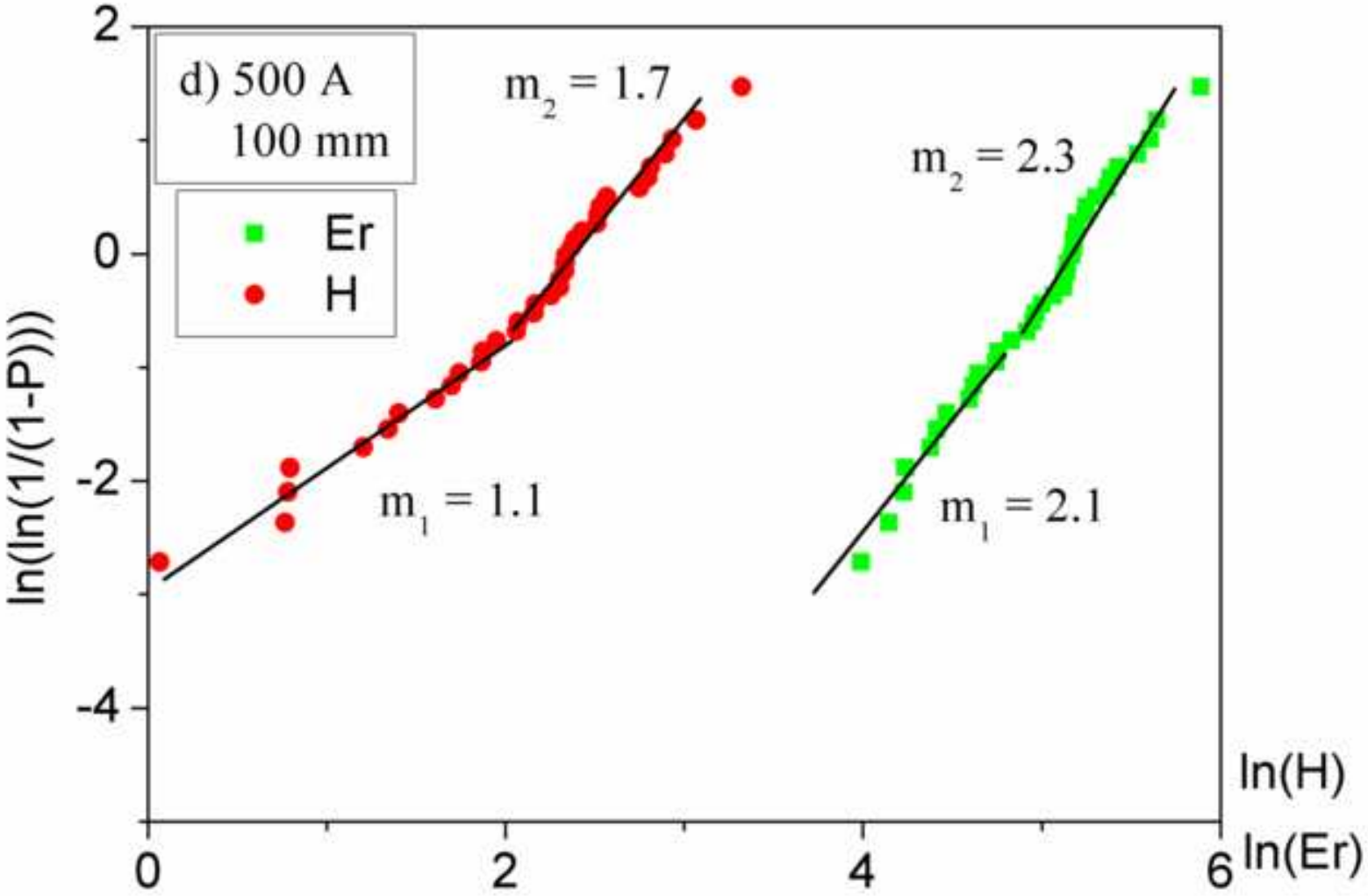

Figure 13(e)
Click here to download high resolution image

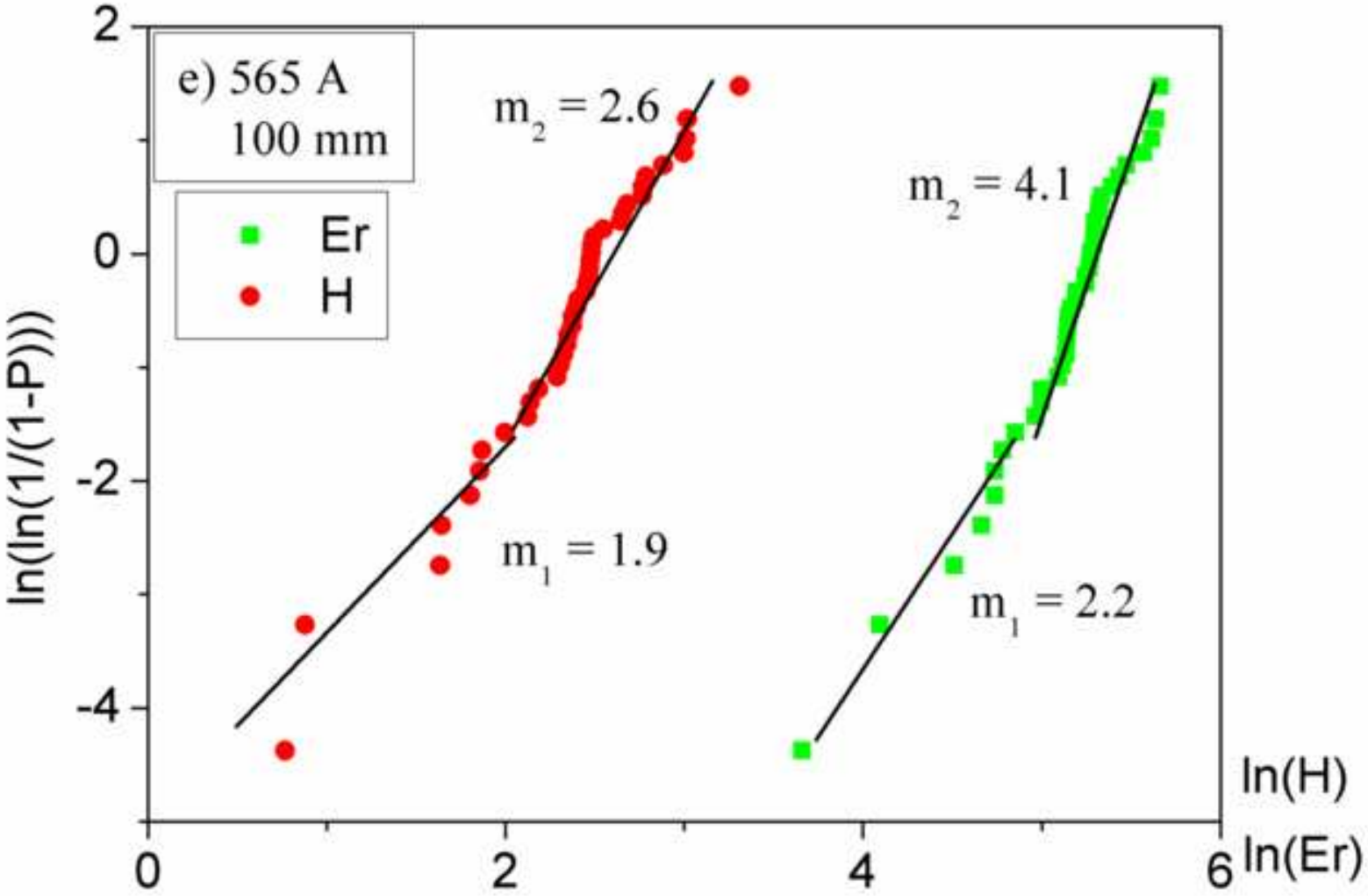

Figure 13(f)
Click here to download high resolution image

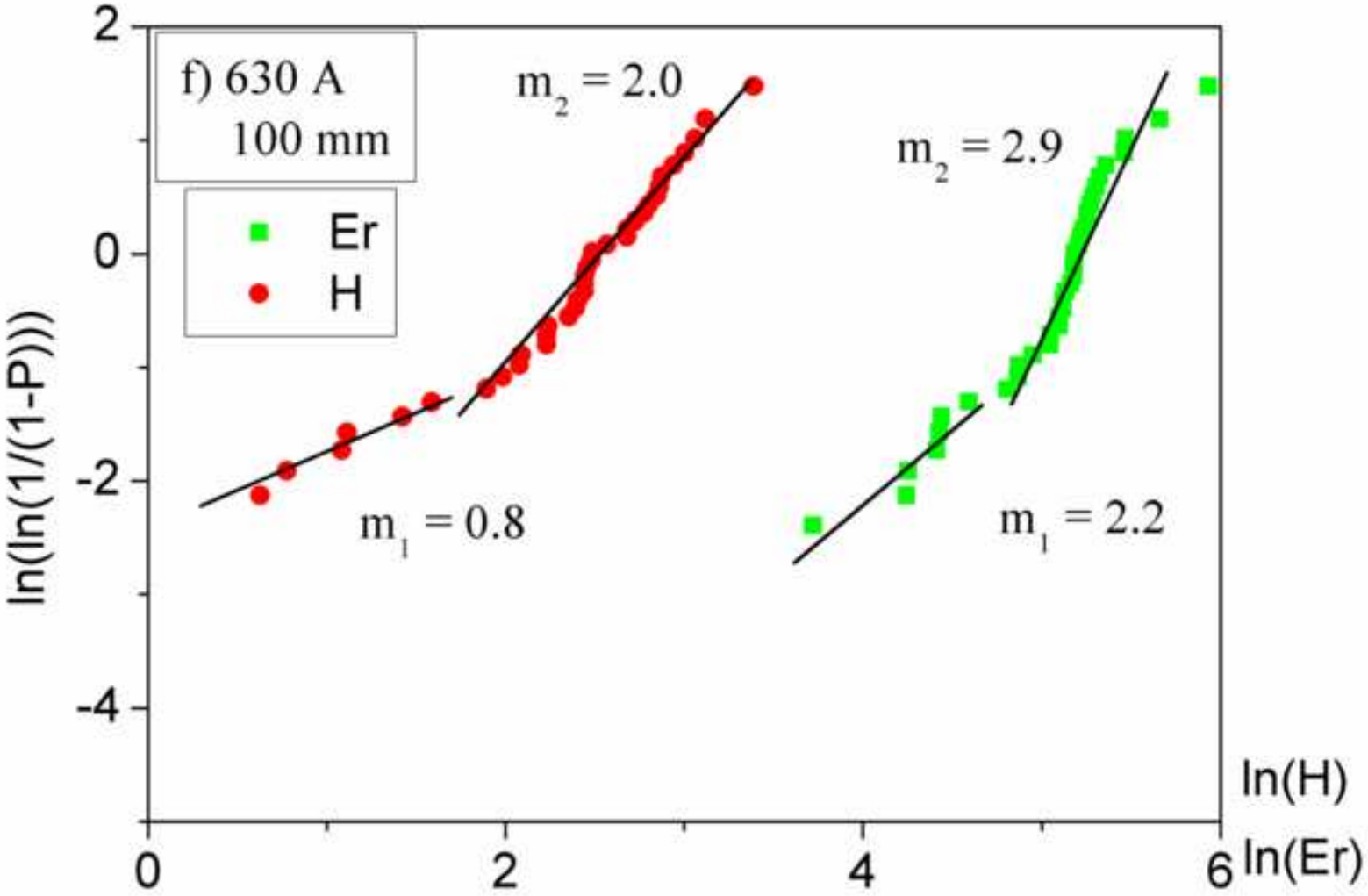

Figure 14(a)
Click here to download high resolution image

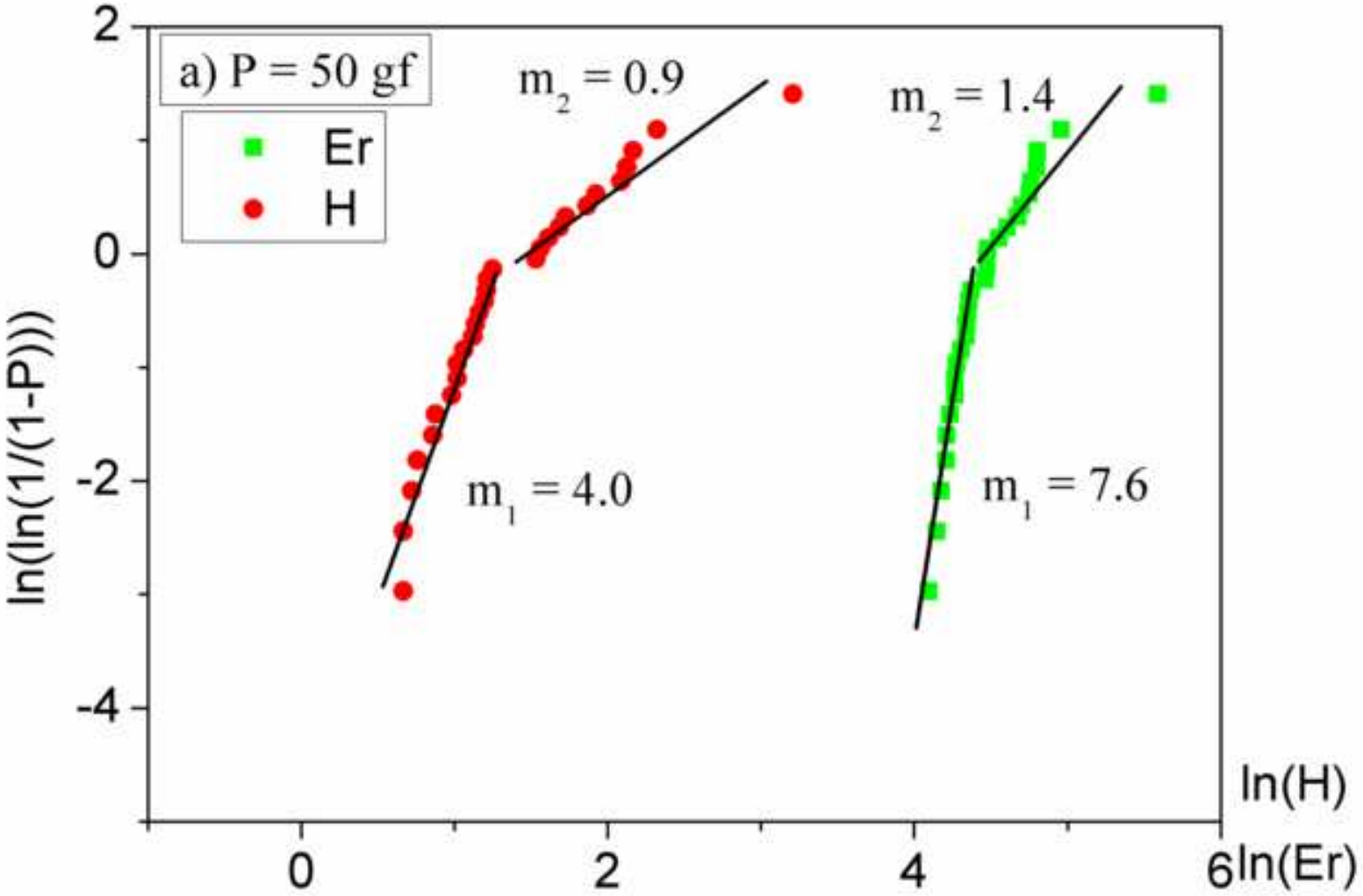

Figure 14(b)
Click here to download high resolution image

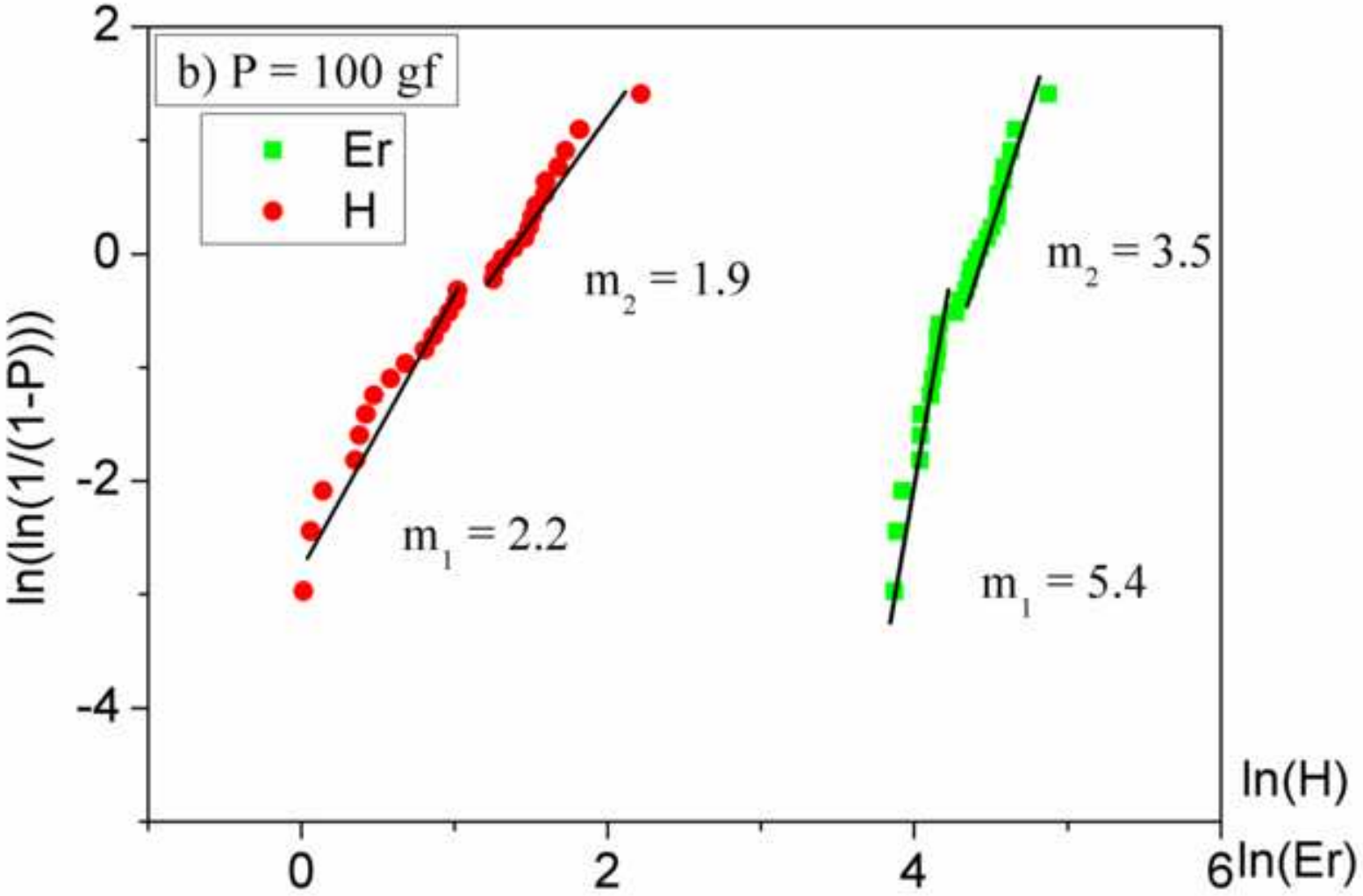

Figure 15
Click here to download high resolution image

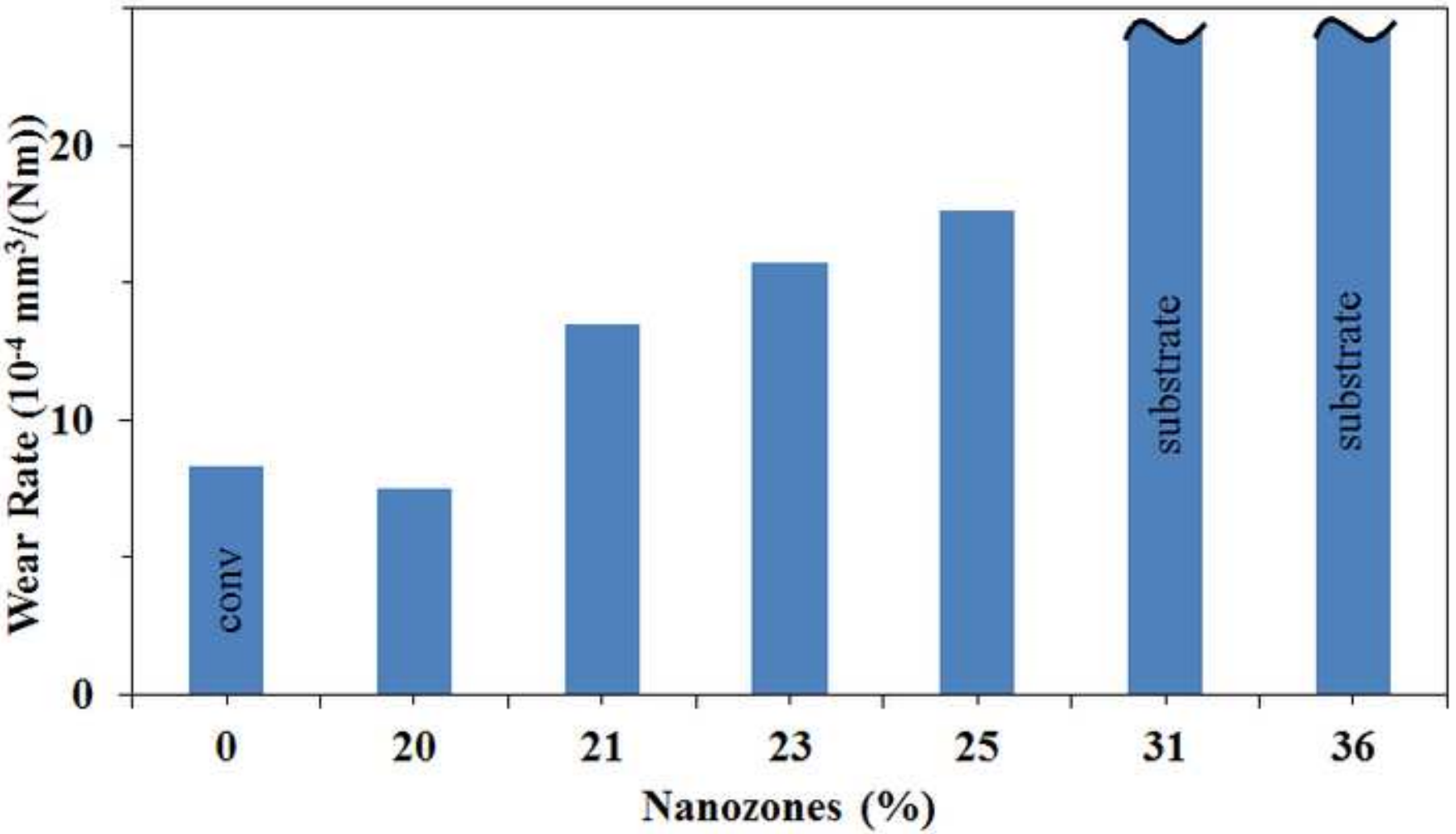

Figure 16(a)
Click here to download high resolution image

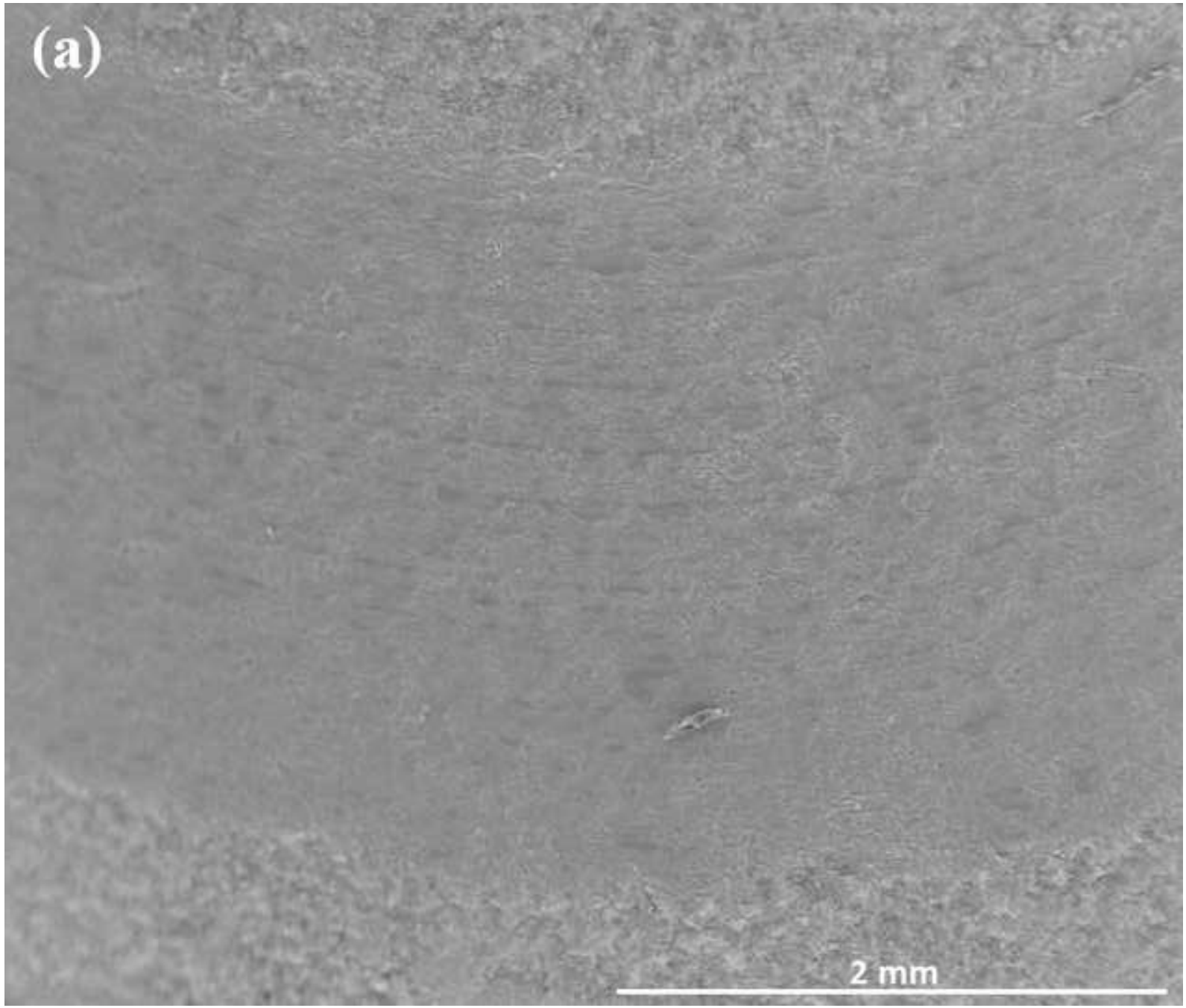

Figure 16(b)
Click here to download high resolution image

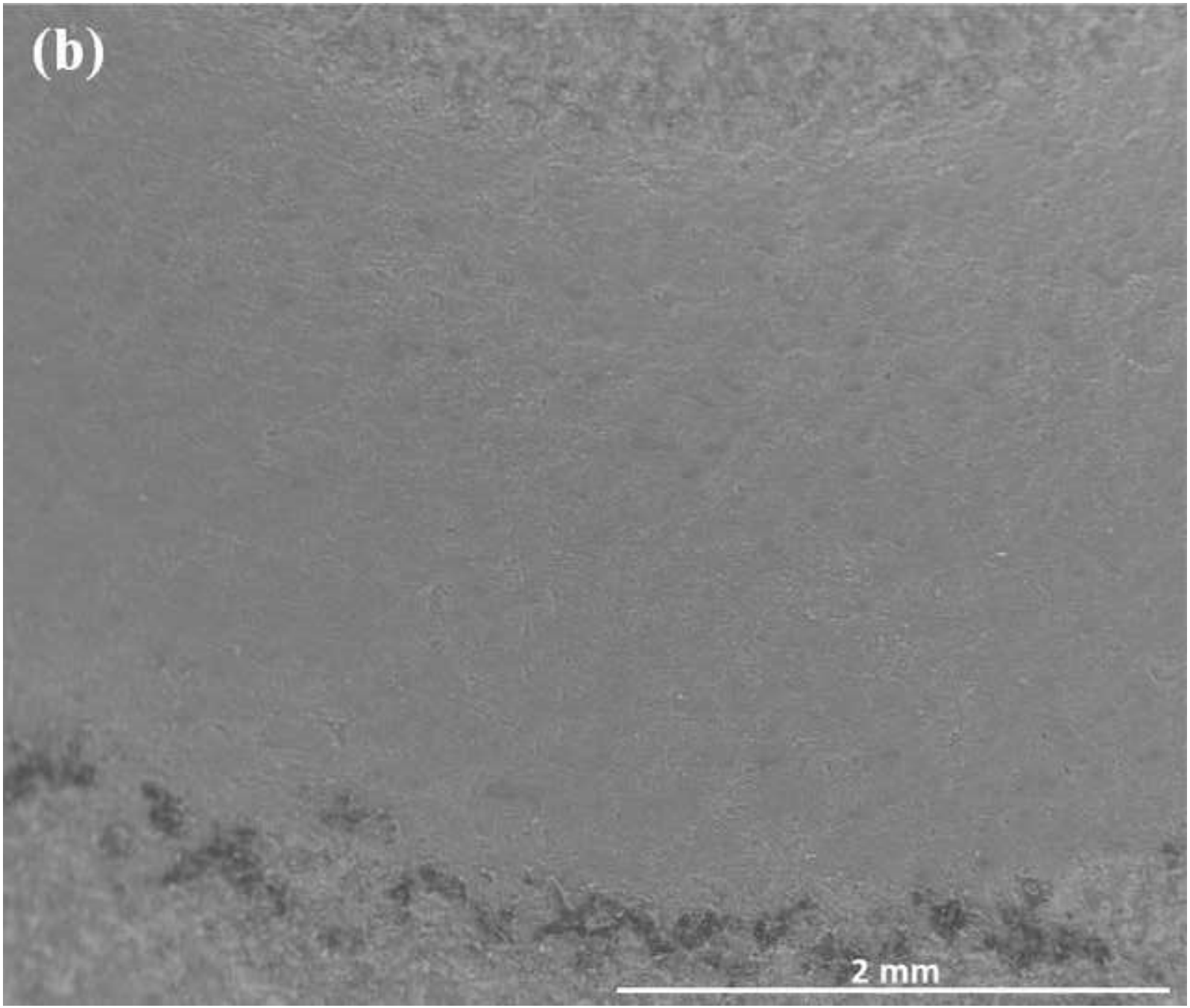

Figure 16(c)
Click here to download high resolution image

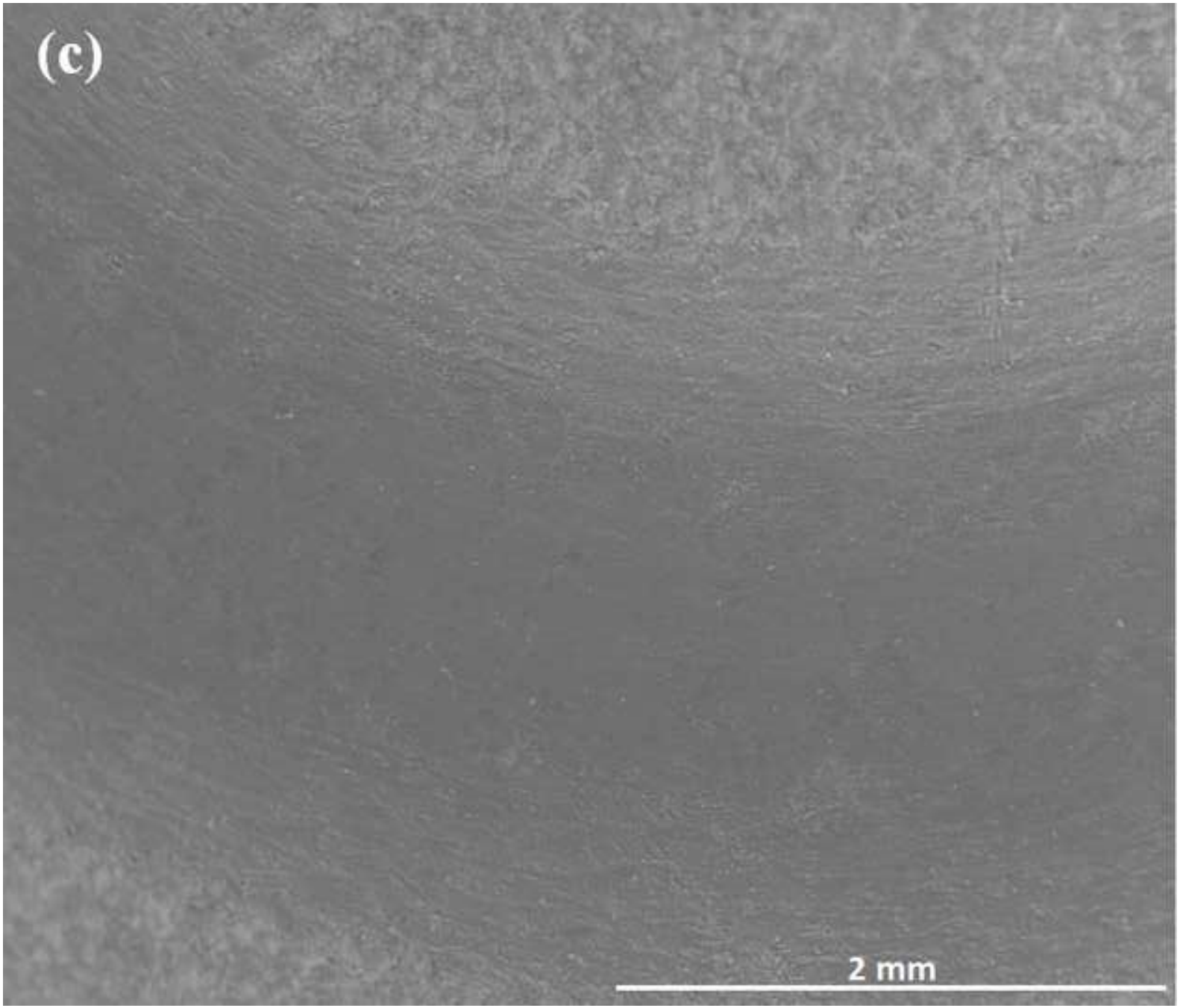

Figure 17(a)
Click here to download high resolution image

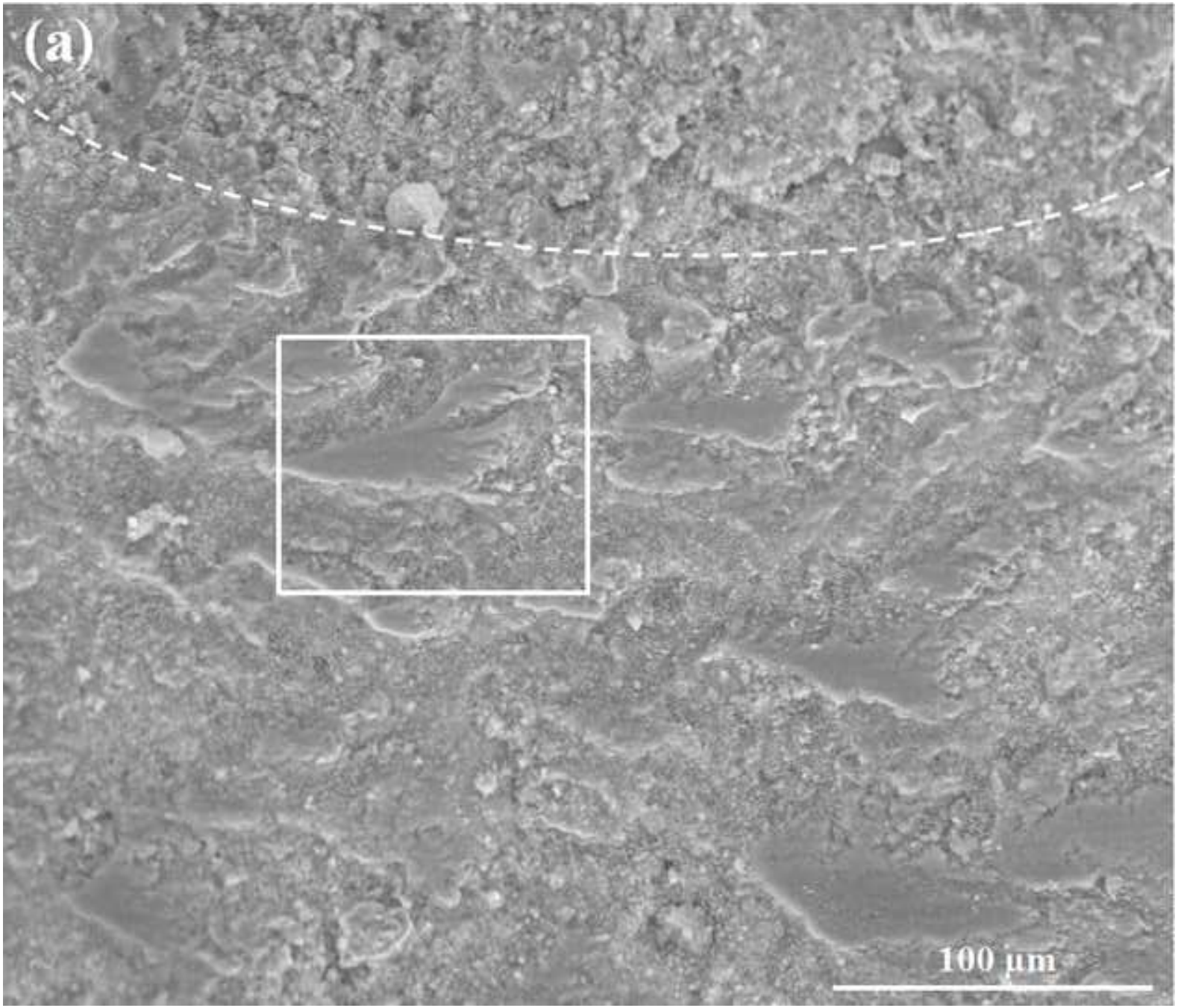

Figure 17(b)
Click here to download high resolution image